SANDIA REPORT

SAND2012-2161
Unlimited Release
Printed April, 2012

A new time-dependent analytic model for radiation-induced photocurrent in finite 1D epitaxial diodes

Bert Kerr, Carl L. Axness, Jason C. Verley, Charles E. Hembree, and Eric R. Keiter

Prepared by
Sandia National Laboratories
Albuquerque, New Mexico 87185 and Livermore, California 94550

Sandia National Laboratories is a multiprogram laboratory managed and operated by Sandia Corporation, a wholly owned subsidiary of Lockheed Martin Company, for the United States Department of Energy's National Nuclear Security Administration under Contract DE-AC04-94-AL85000.

Approved for public release; further dissemination unlimited.

Sandia National Laboratories

Issued by Sandia National Laboratories, operated for the United States Department of Energy by Sandia Corporation.

NOTICE: This report was prepared as an account of work sponsored by an agency of the United States Government. Neither the United States Government, nor any agency thereof, nor any of their employees, nor any of their contractors, subcontractors, or their employees, make any warranty, express or implied, or assume any legal liability or responsibility for the accuracy, completeness, or usefulness of any information, apparatus, product, or process disclosed, or represent that its use would not infringe privately owned rights. Reference herein to any specific commercial product, process, or service by trade name, trademark, manufacturer, or otherwise, does not necessarily constitute or imply its endorsement, recommendation, or favoring by the United States Government, any agency thereof, or any of their contractors or subcontractors. The views and opinions expressed herein do not necessarily state or reflect those of the United States Government, any agency thereof, or any of their contractors.

Printed in the United States of America. This report has been reproduced directly from the best available copy.

Available to DOE and DOE contractors from
U.S. Department of Energy
Office of Scientific and Technical Information
P.O. Box 62
Oak Ridge, TN 37831

Telephone:	(865) 576-8401
Facsimile:	(865) 576-5728
E-Mail:	reports@adonis.osti.gov
Online ordering:	http://www.osti.gov/bridge

Available to the public from
U.S. Department of Commerce
National Technical Information Service
5285 Port Royal Rd
Springfield, VA 22161

Telephone:	(800) 553-6847
Facsimile:	(703) 605-6900
E-Mail:	orders@ntis.fedworld.gov
Online ordering:	http://www.ntis.gov/help/ordermethods.aspx#online

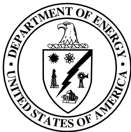

SAND2012-2161
Unlimited Release
Printed April, 2012

A new time-dependent analytic model for radiation-induced photocurrent in finite 1D epitaxial diodes

Bert Kerr
Mathematics Department
New Mexico Institute of Mining and Technology
Socorro, NM 87801

Carl L. Axness
Advanced Systems Analysis Department

Charles E. Hembree
Radiation Effects Research Department

Jason C. Verley and Eric R. Keiter
Electrical Systems Modeling Department

Sandia National Laboratories
P.O. Box 5800
Albuquerque, NM 87185-1323

Abstract

Photocurrent generated by ionizing radiation represents a threat to microelectronics in radiation environments. Circuit simulation tools such as SPICE [1] can be used to analyze these threats, and typically rely on compact models for individual electrical components such as transistors and diodes. Compact models consist of a handful of differential and/or algebraic equations, and are derived by making simplifying assumptions to any of the many semiconductor transport equations. Historically, many photocurrent compact models have suffered

from accuracy issues due to the use of qualitative approximation, rather than mathematically correct solutions to the ambipolar diffusion equation. A practical consequence of this inaccuracy is that a given model calibration is trustworthy over only a narrow range of operating conditions. This report describes work to produce improved compact models for photocurrent. Specifically, an analytic model is developed for epitaxial diode structures that have a highly doped subcollector. The analytic model is compared with both numerical TCAD calculations, as well as the compact model described in reference [2]. The new analytic model compares well against TCAD over a wide range of operating conditions, and is shown to be superior to the compact model from reference [2].

Acknowledgements

The authors acknowledge the support of the Advanced Simulation and Computing (ASC) research programs at the U.S. Department of Energy.

Contents

1 Introduction 11
1.1 Drift-Diffusion Formulation 11
1.2 Ambipolar Diffusion Equation 12
1.3 Photocurrent in Epitaxial Structures 13
2 Mathematical Development 15
2.1 Steady-State Solution 16
2.2 Transient Solution 18
3 Code Comparisons 21
3.1 Comparisons for an Ideal Epitaxial Device 22
3.2 Comparison for a Realistic Epitaxial Device, the 2N2222 Transistor 28
4 Conclusions 41

Appendix

A Transient Excess Carrier and Photocurrent Solution Development 45
B Limiting Behavior of Photocurrent Solutions 51
B.1 Comparison with the Long, Florian, and Casey [3] Steady-State Solution 51
B.2 Comparison with the Stuetzer [4] Steady-State Solution 52
C Evaluation of the Excess Carrier and Photocurrent Densities for a General Piecewise Linear $g(t)$ 53

Figures

1 Reverse-biased 1D abrupt junction pnn^+ diode under irradiation 16
2 Normalized steady-state excess minority carrier density in an irradiated nn^+ region for various dose rates 23
3 Normalized steady-state excess minority carrier density for irradiated nn^+, $n+$ and n regions 24
4 Normalized analytic and TCAD photocurrent densities for the nn^+ region as a function of time for a long irradiation 25
5 Normalized analytic and TCAD photocurrent densities for nn^+, n^+ and n regions for a long irradiation 26
6 Normalized analytic and TCAD photocurrent densities for the nn^+ region as a function of the substrate width for a long irradiation 27
7 Normalized transient TCAD and analytic transient photocurrent densities from the nn^+ region for a short irradiation pulse 27
8 Short and long time scale normalized TCAD and analytic photocurrent densities for the pnn^+ diode with a long radiation pulse 28
9 Sawtooth generation function used for comparison of TCAD, analytic and Xyce codes. 29
10 Comparison of excess minority carrier densities in the 1D abrupt junction nn^+ collector and subcollector regions of the 2222 diode 31
11 The numerically-computed electric field in the 1D abrupt junction nn^+ collector and subcollector regions of the 2222 diode for 0 V, -5 V, and -10 V biases 32
12 Comparison of the minority carrier photocurrent density from the 1D abrupt junction nn^+ collector and subcollector regions of the 2222 diode 33
13 Comparison of the minority carrier photocurrent density from the 1D abrupt junction nn^+ collector and subcollector regions of the 2222 diode, where the generation function time scale is divided by 100 34
14 2N222 BJT within the circuit used in radiation testing 35
15 Comparison of the photocurrent density from the 2222 computed using the Sentaurus TCAD simulator, the analytic code, and the Xyce circuit simulator for the generation function given in Figure 9 36
16 Comparison of the photocurrent density from the 2222 computed using the Sentaurus TCAD simulator, the analytic code, and the Xyce circuit simulator for the generation function given in Figure 9, time-compressed by a factor of 100 37
17 Comparison of the photocurrent density from the 2222 computed using the Sentaurus TCAD simulator, the analytic code, and the Xyce circuit simulator for the generation function given in Figure 9, time-compressed by a factor of 1000 38
18 Comparison of the photocurrent density from the 2222 computed using the Sentaurus TCAD simulator, the analytic code, and the Xyce circuit simulator for the generation function given in Figure 9, time-expanded by a factor of 10 39

Tables

1 Definition and description of important physical constants and parameters. 13
2 Parameters selected for the ideal device. 22
3 2222 physical parameters 30
4 2222 widths used in the analytic model 30

1 Introduction

Circuit simulators, such as SPICE [1] or Xyce [5], are often used to analyze circuit-level photocurrent effects generated by ionizing radiation. Circuit simulators typically rely on compact models for modeling the individual circuit components [6]. Such models are very small and efficient, but are of relatively low fidelity, and rely heavily on calibration and empirical approximations. For example, the photocurrent radiation models currently employed in Xyce are based on the compact model presented in reference [2]. Similar to many compact models, the model presented in [2] relies on empirical assumptions, particularly for handling the delay terms of the model.

In contrast to compact models, device simulators—often referred to as TCAD (Technology Computer-Aided Design) simulators (e.g., [7], [8])—are capable of simulating individual transistors at a much higher level of fidelity. Typically, simulators of this style use the drift-diffusion (DD) formulation discretized over a multi-dimensional numerical mesh. While this style of simulation is higher fidelity, and presumably more accurate than a compact model, it is also several orders of magnitude more computationally expensive. TCAD-style simulators are often coupled to circuit simulators [9], but the high computational costs make simulation of more than a handful of devices prohibitive. Thus, there is motivation to develop fast running compact models, but with the fidelity approaching that of TCAD.

In many practical applications, photocurrent is generated in one-dimensional (or nearly one-dimensional) structures in semiconductor devices. Examples include reverse-biased PN junctions (such as the base-collector of a BJT) and the drain-body regions of MOSFETs. These devices are often constructed with epitaxial layers, so to first order these regions may be analyzed by one-dimensional models. This is a typical approximation used in compact models, but can also be used to expedite TCAD calculations.

1.1 Drift-Diffusion Formulation

The transport behavior of excess carriers in semiconductors can be described using the well-known drift-diffusion (DD) equations [10], [11]. (Other transport formulations exist, but DD is the one most commonly used in device simulation.) This formulation consists of three coupled PDE's: a single Poisson equation for the electrostatic potential and two continuity equations, one each for electrons and holes. They are given by:

$$-\nabla \cdot (\varepsilon \nabla \phi) = q\left[p - n + C\right] \tag{1}$$

$$\frac{\partial n}{\partial t} = \nabla \cdot \left[n \mu_n \mathbf{E} + D_n \nabla n\right] - R + g \tag{2}$$

$$\frac{\partial p}{\partial t} = -\nabla \cdot \left[p \mu_p \mathbf{E} - D_p \nabla p\right] - R + g \tag{3}$$

The right hand side of equation (1) is the charge density, which, for semiconductor devices, is determined by the local carrier densities and the local doping. p is the concentration of holes, n is the concentration of electrons, and q is the unit charge. C is the total doping concentration, which

can also be represented as $C = N_D^+ - N_A^-$, where N_D^+ is the concentration of positively ionized donors and N_A^- is the concentration of negatively ionized acceptors.

The continuity equations, (2) and (3), relate the time rate-of-change of the species concentrations to their drift ($n\mu_n\mathbf{E}$ and $p\mu_p\mathbf{E}$) and diffusion ($D_n\nabla n$ and $D_p\nabla p$) currents, and to the destruction and creation of the carriers ("recombination/generation"). R is the recombination rate and g is the generation rate, which are the same for both species. μ_n and μ_p are the mobilities for electrons and holes, respectively, and D_n and D_p are the respective diffusion constants. $\mathbf{E}$ is the electric field, which can be calculated from the gradient of the potential as $\mathbf{E} = -\nabla\phi$.

1.2 Ambipolar Diffusion Equation

Equations (1)-(3) are not amenable to exact analytic mathematical techniques, so most photocurrent compact models (e.g., [2] [3] [4] [12] [13] [14] [15] [16]) use the ambipolar diffusion equation (ADE) to model the behavior of excess carriers in the undepleted regions of a device. The ADE and related ideas originally appeared in the plasma literature, but were first suggested for semiconductors by Van Roosbroeck [17].

Note that photocurrent from the undepleted regions of a semiconductor device (to which the ADE is typically applied) constitutes the "delay" portion of a photocurrent model. Photocurrent from the depleted regions of a device (the so-called "prompt" photocurrent) is generally handled using different approximations. For examples of depletion region photocurrent, see section III of [16] and equation (53) of [14].

The ambipolar diffusion equation is based on two approximations. The first is the electrical neutrality, or charge balance approximation, which states that the excess electron and hole densities are equal across the entire domain. The second approximation is the congruence assumption, where the flux of electrons and holes out of any region must be equal. These assumptions allow one to combine equations (1), (2) and (3) into the single ambipolar diffusion equation (pp. 327-328 [11]). The ADE is given by:

$$\frac{\partial u}{\partial t} = D_a\nabla^2 u - \mu_a\mathbf{E}\cdot\nabla u - \frac{u}{\tau} + g \tag{4}$$

u is the excess carrier density (electrons or holes), D_a is the ambipolar diffusion constant, μ_a is the ambipolar mobility, g is the creation rate for electron-hole pairs and τ is the carrier lifetime. Note that these parameters are all *ambipolar* parameters, as opposed to the *free* parameters used by equations (1), (2) and (3). A full list of the ambipolar and free parameters used in this work is given in Table 1.

Many of the ambipolar parameters depend upon the excess carrier density, making the ADE a nonlinear equation. However, in the case where the radiation generation density is low-level, the ambipolar parameters become approximately constant and the ADE becomes linear. The range over which the radiation generation density is low-level depends upon the equilibrium (pre-radiation) density of holes (p-type) or electrons (n-type) in the device region, which, in turn depend upon the

Table 1: Definition and description of important physical constants and parameters.

Constant	Description	Units
G	Generation density per rad in Si (4.3×10^{13})	1/cm^3·rad(Si)
q	Electronic charge (1.602×10^{-19})	C
k	Boltzmann constant (1.381×10^{-23})	J/K
Parameter	**Description/Equation**	**cgs units**
J_n	Minority carrier current density from the undepleted p region	A/cm^2
J_{pp}	Minority carrier current density from the undepleted nn^+ region	A/cm^2
J_{depl}	Current density from the depleted zone	A/cm^2
$n(x,t)$	Electrons per unit volume	1/cm^3
$p(x,t)$	Holes per unit volume	1/cm^3
$p_0(x)$, $n_0(x)$	Equilibrium hole or electron density, respectively	1/cm^3
τ_p, τ_n	Hole or electron lifetime, respectively	s
μ_p, μ_n	Hole or electron mobility, respectively	cm^2/V·s
D_p, D_n	Hole or electron diffusion coefficient, respectively	cm^2/s
L_p, L_n	Hole or electron diffusion length, $\sqrt{D_p \tau_p}$ or $\sqrt{D_n \tau_n}$, respectively	cm
$u(x,t)$	Excess carriers per unit volume, $p(x,t) - p_0(x)$ or $n(x,t) - n_0(x)$	1/cm^3
D_a	Ambipolar diffusion coefficient, $\frac{(n+p)D_n D_p}{nD_n + pD_p}$	cm^2/s
D_1	Minority carrier diffusion coefficient in the epitaxial region	cm^2/s
D_2	Minority carrier diffusion coefficient in the substrate region	cm^2/s
μ_a	Ambipolar mobility, $\frac{(n_0 - p_0)\mu_n \mu_p}{n\mu_n + p\mu_p}$	cm^2/V·s
N_1	Majority carrier doping in the epitaxial region	1/cm^3
N_2	Majority carrier doping in the substrate region	1/cm^3
τ_a	Ambipolar lifetime, $\frac{p_0+u}{\tau_p} - \frac{p_0}{\tau_{p_0}} = \frac{n_0+u}{\tau_n} - \frac{n_0}{\tau_{n_0}}$	s
τ_1	Minority carrier lifetime in the epitaxial region	s
τ_2	Minority carrier lifetime in the substrate region	s
W	Depletion width	cm
$\dot{\gamma}$	Dose rate	rad(Si)/s
g	Generation density, $G \cdot \dot{\gamma}$	1/cm^3·s

doping concentration. Low-level radiation conditions are defined to be $u << n_0$ for n-type doped material and $u << p_0$ for p-type material, where n_0 and p_0 are the equilibrium electron and hole densities, respectively (see pg. 328, [11]). In this study, the one-dimensional (1D) ADE is solved in the undepleted n and n^+ regions of a reverse-biased pnn^+ diode. In these regions, the electric field in the ADE is an ohmic field imposed by a voltage bias applied at the device contacts. For explicitly-doped devices, the ambipolar parameters become the minority carrier parameters and the photocurrent is dominated by the minority carrier current. For devices with significant doping, this electric field is small and may be ignored (see pp. 330-333, [11]).

1.3 Photocurrent in Epitaxial Structures

The focus of this work is the development of new mathematical solutions for the ADE in doped epitaxial structures. The new solutions build upon the mathematical framework presented in [16], [18] and [19]. An epitaxial structure is fairly common in silicon-based BJTs and CMOS devices. It

may be used to enhance the performance of a device by electrically isolating the epitaxial structure with an oppositely doped substrate. In addition, a thin, highly-doped layer can be added at the substrate-epitaxial interface, which reduces device resistance. Finally, a substrate that is highly doped relative to the epitaxial layer can aid in reducing radiation effects by reducing the minority carrier lifetimes in the substrate. This limits the collection of excess carriers generated by ionizing radiation in the substrate, and thus reduces the excess carriers diffusing to the device active regions.

Generally, we are interested in the photocurrent generated by pnn^+ diodes under reverse bias, which is the focus of this report. However, the solution derived herein also applies to an npp^+ diode. At present, we are aware of only one analytic ADE solution that has evaluated radiation generated photocurrent by solving the excess carrier density in epitaxial devices. The Long, Florian, and Casey (LFC) model [3] was developed in 1983. In that work, the ADE was solved to determine photocurrent from an irradiated pnn^+ diode under steady-state conditions, assuming an infinitely-extending n^+ substrate and a constant radiation generation density. An approximate solution for the transient problem was given for a boundary condition that suppressed the current from the substrate to the n region.

In addition to the LFC model [3], the Fjeldly model [2] also purports to treat the subcollector. However, the Fjeldly model is not based on a rigorous solution of the ADE. Subcollector effects are accommodated by assuming that the addition of a highly doped vertical subcollector will restrict photocurrent collection to within one diffusion length of the subcollector boundary, and accordingly adjusting the area and volume prefactors applied to the "delay" portion of the model.

Similar to previous work ([16], [18], [19] and [20]), we use the finite Fourier transform technique [21] to solve the (1D) ADE and derive the exact transient carrier density in, and associated photocurrent from, the unbiased nn^+ sub-component of an epitaxial diode experiencing a radiation transient. We show that our steady-state photocurrent solution for the nn^+ region approaches the solution of Long, Florian and Casey [3], as well the Stuetzer steady-state photocurrent solution [4], as the relevant parameters approach those of the respective models. Our transient solution improves on that of [3], since it uses the correct nn^+ boundary conditions, is the solution for a finite diode, and takes into account an arbitrary time-dependent radiation generation density. We also develop the analytical solution for a piecewise linear generation function so that it may be used to analyze realistic pulses, including those based on experimental data.

We also compare the analytic solution to results from TCAD and Xyce calculations, the latter of which uses the Fjeldly model [2]. The comparison begins with an examination of the excess carrier density and photocurrent of a model pnn^+ diode, with particular attention paid to the diode's unbiased nn^+ sub-component. The influence of the substrate width on the photocurrent for this device is also explored. We conclude by examining the excess carrier density and photocurrent generated in a device whose doping and geometry parameters are based on the 2N2222 bipolar junction transistor, a commercially available part.

2 Mathematical Development

Determination of the photocurrent contribution from the undepleted regions of a diode requires us to solve the ambipolar diffusion equation (given in equation (4)). Figure 1 shows the depleted and undepleted regions of a reverse-biased 1D abrupt junction pnn^+ diode under irradiation, along with the coordinate systems used for deriving the analytic solution. It is worth noting that the following derivation for a pnn^+ diode can be applied to an npp^+ device by simply reversing the n and p subscripts. All the parameters used in this section are described in Table 1.

Several simplifying assumptions were made to make the solution to the ADE more tractable. In particular, we wanted to make the solution easily implemented as a compact model, balancing accuracy with computational complexity. Therefore, we first restricted the ADE to one dimension. (While many electronic devices are inherently multi-dimensional in nature, the epitaxial structures targeted by this model lend themselves to a 1D analysis.) Next, we assumed the different regions of the diode had constant doping levels. This results in constant mobilities and diffusion coefficients in each region. (If the doping levels were spatially dependent, the mobilities and diffusion coefficients would be functions of position, thus complicating the solution to the ADE.) The diode was also assumed to be strongly extrinsic (highly-doped), such that the photocurrent from the undepleted regions is dominated by the excess minority carriers, and the ambipolar parameters become the minority carrier parameters in the undepleted regions. Additionally, we approximated the boundary widths of the depleted and undepleted regions by the abrupt pn diode depletion region approximation ([22], pp. 74 – 77). While the formula was not derived for a pnn^+ device, it is a good approximation for devices where the depletion zones due to the nn^+ and pn interfaces do not overlap. Finally, we make the assumption that the electric field is negligible in the undepleted regions of the device.

For a reverse-biased 1D pnn^+ diode, the total photocurrent may be written as the sum of the photocurrents generated in each region,

$$J_{total} = J_n + J_{depl} + J_{pp} \tag{5}$$

A simple analytic approximation for the depletion region current is $J_{depl} = qg(t)W$. This approximation assumes that all charge deposited in the depleted region is collected instantaneously by the electric field, with no excess carrier recombination. The photocurrent in the irradiated homogeneous undepleted p region has been solved in [16]. We now proceed by determining the photocurrent in the nn^+ region. In the undepleted n region, the excess minority carrier density may be found by solving the equation (cf. equation (4), with $\mathbf{E} = \mathbf{0}$),

$$u_t = D_1 u_{xx} - \tfrac{1}{\tau_1} u + g(t) \quad , \quad 0 \le x \le w_1 \tag{6}$$

where the parameters are given in Table 1. Similarly, in the epitaxial region the equation,

$$u_t = D_2 u_{xx} - \tfrac{1}{\tau_2} u + g(t) \quad , \quad w_1 \le x \le w_2 \tag{7}$$

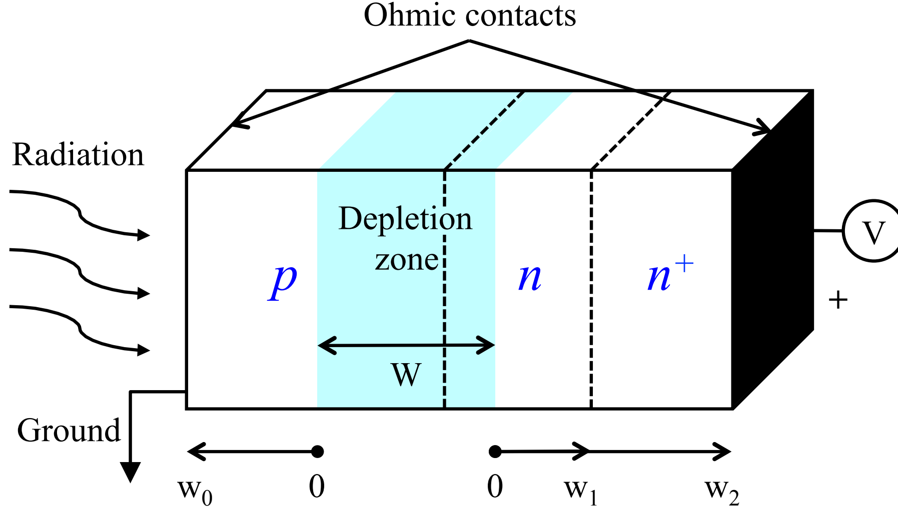

Figure 1: The depleted and undepleted regions of a reverse-biased 1D abrupt junction pnn^+ diode under irradiation, along with the coordinate systems used for deriving the analytic solution. The radiation generation is assumed to be uniform throughout the device.

is assumed. The boundary conditions are:

$$u(0,t) = 0 \tag{8}$$

$$u(w_2,t) = 0 \tag{9}$$

$$D_1 \frac{\partial u}{\partial x}\bigg|_{x=w_1^-} = D_2 \frac{\partial u}{\partial x}\bigg|_{x=w_1^+} \tag{10}$$

$$N_1 u(w_1^-,t) = N_2 u(w_1^+,t) \tag{11}$$

where w_1 is the undepleted thickness of the epitaxial region and w_2 is the undepleted thickness of both the epitaxial region and the substrate. The third boundary condition requires that the excess carrier current be continuous through the nn^+ junction, and the fourth boundary condition requires that the ratio of the excess carrier density on each side of the junction remains fixed at a value dictated by the ratio of the majority carrier concentrations, N_1 and N_2. This boundary condition was suggested in [3], and we have verified that it holds when the nn^+ boundary is sufficiently far from the *pn* depletion region through the comparison shown in Figure 2 in Section 3.1. The initial condition is assumed to be

$$u(x,0) = 0 \quad , \quad 0 < x < w_2 \tag{12}$$

2.1 Steady-State Solution

For steady-state equilibrium conditions (assuming $g(t) = g, t \geq 0$), a closed form equation for the excess carrier density can be obtained. The general solution to the steady-state diffusion equation

is

$$U(x) = \tfrac{A}{2}e^{\alpha_1 x} + Ce^{-\alpha_1 x} + g\tau_1 \quad , \quad 0 \le x \le w_1$$
$$U(x) = \tfrac{B}{2}e^{\alpha_2(w_2-x)} + Ee^{-\alpha_2(w_2-x)} + g\tau_2 \quad , \quad w_1 \le x \le w_2 \tag{13}$$

where $\alpha_i = \frac{1}{\sqrt{D_i\tau_i}}$, for $i = 1,2$ and we use $U(x)$ to represent the steady-state solution. Using equations (8) and (9) enables us to evaluate C and E, leaving us with,

$$U(x) = A\sinh(\alpha_1 x) + g\tau_1\left[1 - e^{-\alpha_1 x}\right] \quad , \quad 0 \le x \le w_1$$
$$U(x) = B\sinh(\alpha_2(w_2 - x)) + g\tau_2\left[1 - e^{-\alpha_2(w_2-x)}\right] \quad , \quad w_1 \le x \le w_2 \tag{14}$$

For convenience, we relabel this solution as

$$U(x) = AS_1(x) + g\tau_1 G_1(x) \quad , \quad 0 \le x \le w_1$$
$$U(x) = BS_2(x) + g\tau_2 G_2(x) \quad , \quad w_1 \le x \le w_2 \tag{15}$$

Then, to satisfy boundary conditions (10) and (11), we require

$$N_1\left[AS_1(w_1) + g\tau_1 G_1(w_1)\right] = N_2\left[BS_2(w_1) + g\tau_2 G_2(w_1)\right] \tag{16}$$

and

$$D_1\left[AS_1'(w_1) + g\tau_1 G_1'(w_1)\right] = D_2\left[BS_2'(w_1) + g\tau_2 G_2'(w_1)\right] \tag{17}$$

Applying Cramer's rule and solving these equations for A and B it follows that,

$$A = g\frac{N_2S_2(w_1)\left[D_2\tau_2G_2'(w_1) - D_1\tau_1G_1'(w_1)\right] - D_2S_2'(w_1)\left[N_2\tau_2G_2(w_1) - N_1\tau_1G_1(w_1)\right]}{D_1N_2S_1'(w_1)S_2(w_1) - N_1D_2S_1(w_1)S_2'(w_1)} \tag{18}$$

and

$$B = g\frac{N_1S_1(w_1)\left[D_2\tau_2G_2'(w_1) - D_1\tau_1G_1'(w_1)\right] - D_1S_1'(w_1)\left[N_2\tau_2G_2(w_1) - N_1\tau_1G_1(w_1)\right]}{D_1N_2S_1'(w_1)S_2(w_1) - N_1D_2S_1(w_1)S_2'(w_1)} \tag{19}$$

Substituting (18) and (19) into (14) completes the steady-state solution.

The steady-state photocurrent, which we designate as $J_{pp}(\infty)$, can be calculated from

$$J_{pp}(\infty) = qD_1 \left.\frac{\partial U}{\partial x}\right|_{x=0} = qD_1\alpha_1\left(A + g\tau_1\right) \tag{20}$$

In Appendix B we show that our finite steady-state nn^+ photocurrent solution approaches that of [3] as the length of the n^+ region approaches infinity. We also show that the photocurrent approaches the solution of [4] as the doping and parameters in the epitaxial and substrate regions approach each other and the nn^+ zone becomes entirely homogeneous.

2.2 Transient Solution

The general solution of the BVP defined by equations (6)–(12) may be found by the finite Fourier transform method ([16], [21]). However, determining the required eigenvalues and eigenfunctions for this transform is less straightforward than for a homogeneous region. The two composite layers within the region, coupled with the interface boundary conditions (10) and (11), produce a sequence of piecewise continuous eigenfunctions, in which the eigenvalues are given by a transcendental equation. The development is presented in Appendix A.

For an arbitrary time-dependent $g(t)$, the formula for the excess carrier density in the nn^+ region may be written as,

$$u(x,t) = \sum_{n=1}^{\infty} w_n \int_0^t g(v) e^{-\lambda_n (t-v)} dv \frac{X_n(x)}{\|X_n\|^2} \tag{21}$$

The associated photocurrent (defined to be positive for convenience) is given by

$$\begin{aligned} J_{pp}(t) &= qD_1 \left.\frac{\partial u}{\partial x}\right|_{x=0} \\ &= qD_1 \sum_{n=1}^{\infty} w_n \int_0^t g(v) e^{-\lambda_n (t-v)} dv \frac{X_n'(0)}{\|X_n\|^2} \end{aligned} \tag{22}$$

The definitions of w_n, λ_n, $X_n(x)$, and $\|X_n\|^2$ are given in Appendix A. For the case where $g(t) = g$ (a constant), equation (21) reduces to

$$u(x,t) = U(x) - g \sum_{n=1}^{\infty} w_n \frac{e^{-\lambda_n t}}{\lambda_n} \frac{X_n(x)}{\|X_n\|^2} \tag{23}$$

where $U(x)$ is the steady-state solution. The photocurrent density is,

$$J_{pp}(t) = qD_1 \alpha_1 \left[A + g\tau_1 - \frac{g}{\alpha_1} \sum_{n=1}^{\infty} w_n \frac{e^{-\lambda_n t}}{\lambda_n} \frac{X_n'(0)}{\|X_n\|^2} \right] \tag{24}$$

For the case where the carrier generation rate is a step function,

$$g(t) = \begin{cases} g \quad , \quad 0 \le t \le t' \\ 0 \quad , \quad t' < t < \infty \end{cases} \tag{25}$$

equation (21) reduces to

$$u(x,t) = \begin{cases} U(x) - g \sum_{n=1}^{\infty} w_n \frac{e^{-\lambda_n t}}{\lambda_n} \frac{X_n(x)}{\|X_n\|^2} \quad , \quad 0 \le t \le t' \\ g \sum_{n=1}^{\infty} w_n \frac{e^{-\lambda_n (t-t')} - e^{-\lambda_n t}}{\lambda_n} \frac{X_n(x)}{\|X_n\|^2} \quad , \quad t' < t < \infty \end{cases} \tag{26}$$

and the associated photocurrent is given by

$$J_{pp}(t) = \begin{cases} qD_1\alpha_1\left[A + g\tau_1 - \frac{g}{\alpha_1}\sum_{n=1}^{\infty} w_n \frac{e^{-\lambda_n t} X_n'(0)}{\lambda_n \|X_n\|^2}\right] & , \quad 0 \le t \le t' \\ qgD_1 \sum_{n=1}^{\infty} w_n \frac{e^{-\lambda_n (t-t')} - e^{-\lambda_n t}}{\lambda_n} \frac{X_n'(0)}{\|X_n\|^2} & , \quad t' < t < \infty \end{cases} \tag{27}$$

The transient solution converges very quickly, and the analytic simulations reported in the following sections required only a few hundred terms to converge. Observe that the formulas for the excess carriers and photocurrent are linearly dependent upon g. Therefore, a single normalized curve represents all radiation levels. We will use this fact throughout the remaining sections when comparing analytic and TCAD results. For the case of a general piecewise linear $g(t)$, the analogous formulas of (26) and (27) are given in Appendix C.

3 Code Comparisons

In this section, we compare the analytic model to other computational models, which have differing levels of fidelity. The goal of these comparisons is to examine the validity of using the ADE to model photocurrent, and also to provide some evidence that the assumptions made in our analytic model were valid. These comparisons do not include comparisons against experimental data, which is required to fully validate any computational model.

In section 3.1, the analytic model is compared to a TCAD device simulator, Sentaurus [7], for an ideal device. The device has a constant doping in each region, rather than having a spatially-dependent profile, which is more typical in realistic devices. The doping levels and the physical parameters and dimensions were chosen for their simplicity, so as to best elucidate the success or failure of the analytic model in an idealized case. In section 3.2, we perform a similar comparison, but for a realistic commercial device. For the realistic device comparison, we compare the new model to TCAD, and also compare it to the Fjeldly [2] photocurrent model, which is a lower fidelity compact model.

Sentaurus solves the DD equations (equations (1)–(3)) over the entire device. The analytic model is a lower-fidelity formulation than the DD equations, in that its derivation involves several additional approximations. These extra approximations include:

1. The ADE is derived under the electrical neutrality assumptions ([11], [17]).
2. The analytic model assumes that the photocurrent is dominated by the minority carrier diffusion currents from the undepleted regions and the field-driven depletion current.
3. The analytic model assumes a simple photocurrent solution in the depletion region and utilizes an approximation for the boundaries between the depleted and undepleted regions.
4. Simple boundary conditions at the depleted/undepleted boundaries and the nn^+ interface are assumed in the analytical model, which are not exactly met in the TCAD code.
5. The analytic model assumes constant doping levels in each region, whereas that is not required for a TCAD code.

Each of the above assumptions may result in differences between analytic model results and TCAD. By performing this comparison, it is possible to evaluate the consequences of these assumptions, and how they impact the applicability of the ADE.

Some particulars of the Sentaurus calculations are as follows. For this 1D case, the boundary conditions in Sentaurus are required to be defined only at the contacts. (Sentaurus is inherently a 3D code, so reflective boundary conditions are enforced on the surfaces parallel to the x-coordinate.) The contact boundary conditions were chosen to be ohmic, which assumes charge neutrality and equilibrium [7]. Additionally, the analytic solution is in terms of the excess carrier density, while Sentaurus computes only the total electron and hole concentrations within the device. Therefore,

Table 2: Parameters selected for the ideal device.

Input	Description	value	units
N_0	Doping in the p doped region	1×10^{16}	cm^{-3}
N_1	Doping in the n doped region	1×10^{16}	cm^{-3}
N_2	Doping in the n^+ substrate	1×10^{18}	cm^{-3}
τ_0	Minority carrier lifetime, p region	2×10^{-5}	s
τ_1	Minority carrier lifetime, n region	2×10^{-5}	s
τ_2	Minority carrier lifetime, n^+ region	1×10^{-7}	s
w_0	Undepleted length, p region	2.8875×10^{-4}	cm
w_1	Undepleted length, n region	2.8875×10^{-4}	cm
w_2	Undepleted length, n region + n^+ region	1.28875×10^{-3}	cm
W	Abrupt pn depletion width	1.225×10^{-4}	cm
D_0	Minority carrier diffusion coefficient, p region	25.9	cm^2/s
D_1	Minority carrier diffusion coefficient, n region	10.36	cm^2/s
D_2	Minority carrier diffusion coefficient, n^+ region	2.59	cm^2/s
V	Voltage bias across diode	-5	V

we post-process the Sentaurus data by subtracting the pre-irradiation carrier densities from those computed during irradiation to find the excess carrier densities.

3.1 Comparisons for an Ideal Epitaxial Device

In this section the analytic model is compared to TCAD [7] simulations for an ideal device that has constant doping in each region. Recall that the analytic model assumes constant doping levels. By targeting an idealized device for this comparison, one potential source of discrepancy between the analytic model and the TCAD simulations is eliminated.

The parameters used in the analytic model and TCAD simulations are given in Table 2. The depleted and undepleted region widths were calculated from the analytic abrupt diode equations (e.g., see [22], pp. 74 – 77). These are consistent with the depleted and undepleted region widths calculated by Sentaurus from the carrier concentrations.

3.1.1 Steady-State and Long Radiation Pulse Comparisons

Figure 2 illustrates steady-state analytic and TCAD normalized excess minority carrier densities from an unbiased irradiated nn^+ doped silicon region, with parameters as shown in Table 2. Analysis of just the nn^+ region of a pnn^+ diode enables a more accurate validation of the analytic solution, since it avoids the possible errors induced by the addition of currents from the depletion region and the p-doped region.

The nn^+ region is simulated without an applied potential, even though the scenario of interest is a device under reverse bias. This is because the doping levels in this example are high enough that most of the applied potential is dropped across the pn junction, which has been excluded from

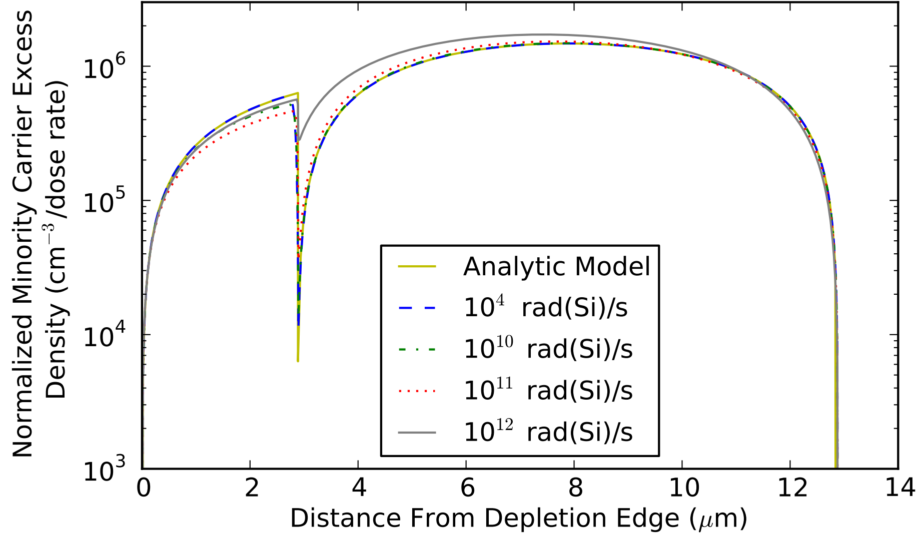

Figure 2: Normalized (with respect to dose rate) steady-state excess minority carrier density for an irradiated nn^+ region as a function of position. The right depletion edge in the pnn^+ diode (Figure 1) would correspond to $x = 0$ in the figure. The densities with dose rate labels are numerically simulated with Sentaurus.

the calculation. Thus, the ohmic fields in the undepleted regions are practically zero. As a result, the unbiased nn^+ calculation gives a good approximation to the photocurrent generated from the undepleted nn^+ region in a reverse-biased pnn^+ device.

The TCAD excess carrier densities in the plot are normalized by the radiation dose rate. Continuous radiation pulses with dose rates between 1×10^4 rad(Si)/s and 1×10^{12} rad(Si)/s were simulated, and are plotted at $t = 1 \times 10^{-4}$ s after pulse initiation, which is well after the excess carrier density achieved a steady state. The TCAD simulations show that the dependence of the excess carrier density on the dose rate is approximately linear for dose rates less than 1×10^{10} rad(Si)/s, and are in close agreement with the analytic solution over this range. Higher dose rates (high-level irradiations) in the TCAD solutions show an increase in the excess carrier density in the n^+ region, and a decrease in the excess carrier discontinuity at the nn^+ interface.

The shape of the analytic and TCAD carrier density curves are similar at the nn^+ interface. The fact that the quasi-discontinuity in the simulated solution is the same order of magnitude in both solutions gives some credence to the assumptions made in the nn^+ interface boundary conditions (equations (10) and (11)). Also, the difference in the minimum value of the interface carrier density may be affected by the mesh-based discretization of the TCAD calculation.

Figure 3 shows a comparison between the new subcollector solution, TCAD, and analytic solutions for two simpler, homogeneous bounding cases. All data in the figure is of normalized excess carrier densities computed for a 1×10^9 rad(Si)/s dose rate. The two bounding cases are normalized analytic steady-state excess carrier densities for n and n^+ homogeneous regions. These regions have the same doping levels as the original nn^+ region, but are either entirely n or n^+ doped.

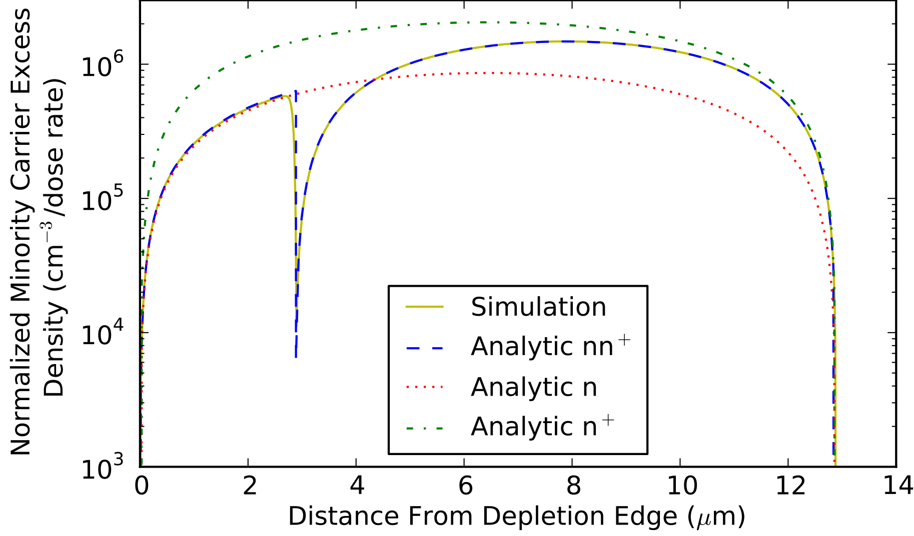

Figure 3: Normalized steady-state excess minority carrier density for irradiated nn^+, n^+ and n regions as a function of position, using the parameters given in Table 2. The plot labeled "simulation" refers to a Sentaurus TCAD simulation at 1×10^9 rad(Si)/s dose rate. The dotted and dot-dashed lines are, respectively, the excess carrier densities for homogenous n and n^+ doped regions computed from the solution of [16].

The homogeneous simulations show that the excess carrier density for the nn^+ region approaches the homogeneous n excess carrier density as one approaches the left contact and the homogeneous n^+ excess carrier density as the right contact is approached. One would expect this behavior in a device where the contacts are located sufficiently far from the nn^+ interface.

Figure 4 is a plot of the photocurrent density coming from the nn^+ region, and illustrates a transition from low radiation levels, where the analytic solution is fairly accurate, to high radiation levels, where the analytic solution starts to diverge from TCAD. This divergence probably occurs because some of the analytic model assumptions are no longer valid. The normalized transient carrier photocurrent density from the nn^+ region due to an infinitely-long radiation pulse is shown in the figure. The photocurrent densities are normalized to a 1×10^9 rad(Si)/s radiation dose rate. The TCAD simulations were performed assuming dose rates from 1×10^4 rad(Si)/s to 1×10^{12} rad(Si)/s. The analytic and TCAD photocurrents between 1×10^4 rad(Si)/s and 1×10^{10} rad(Si)/s essentially overlap. High-level radiation effects become apparent in the TCAD photocurrent simulations when the dose rate exceeds 1×10^{10} rad(Si)/s, and the photocurrent becomes superlinear with respect to g.

Comparison of the normalized analytic result with the TCAD result shows the analytic photocurrent to be highly accurate for low-level irradiations. In fact, the steady-state normalized photocurrent for a 1×10^9 rad(Si)/s dose rate was computed as 4.62673 A/cm^2 using equation (20), and Sentaurus computed the photocurrent as 4.62454 A/cm^2 at $t = 1 \times 10^{-4}$ s. Even at the highest simulated radiation level the difference between the TCAD photocurrent density and the analytic photocurrent density is less than 30%. Examination of the TCAD-computed excess carrier den-

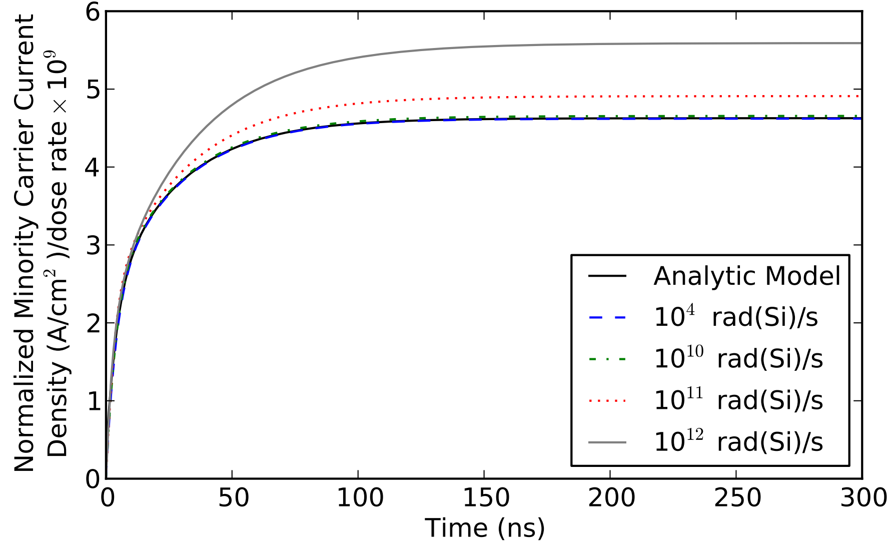

Figure 4: The normalized analytic and TCAD photocurrent densities for the nn^+ region as a function of time for a long irradiation.

sity, electric field, and electron and hole densities (not shown here) at 1×10^{12} rad(Si)/s dose rate, for example, reveal a reduced transition region width from equilibrium (a violation of boundary condition given by equation (11)), non-zero and non-uniform electric fields outside the depletion region, and an excess minority carrier density that is higher than the doping in the n region. These effects are either not considered, or are in violation of the assumptions of the analytic photocurrent model, so a significant error at very high radiation levels is to be expected. Our results show that there is very little error in using the ADE for simulation of photocurrent in lieu of the complete set of transport equations for the nn^+ region at low-level irradiation levels.

Figure 5 illustrates the transient analytic and TCAD photocurrent densities of the nn^+ region at a 1×10^9 rad(Si)/s dose rate, along with two bounding cases. The two bounding cases are for undepleted homogeneous n and n^+ regions, computed using the photocurrent solution of [16], and are shown as dotted and dashed lines. The currents are close to steady-state at 300 ns in all the simulations. The large difference between the homogeneous n and n^+ photocurrents is due to the difference in the depletion length, $\sqrt{D\tau}$, for these simulations. The plot shows that the nn^+ photocurrent is dominated by the n-doped region and that the use of the n^+ substrate for this particular device results in a slightly higher steady-state photocurrent density for the nn^+ simulation than the homogenous n-doped simulation.

Figure 6 illustrates the transient analytic and TCAD nn^+ region simulated minority carrier photocurrent densities for varying widths of the n^+ substrate region ($w_2 - w_1$). The radiation dose rate is 1×10^9 rad(Si)/s, and the substrate width is indicated on the right side of the figure. The analytic and TCAD plots essentially overlap in each case. It is apparent that, for the parameters and doping levels used in these nn^+ simulations, a significant amount of charge is collected from deep within the substrate, to a depth of between 20–30 μm. The steady-state photocurrent for a long radiation pulse, ($g(t) = g, t \geq 0$), from a nn^+ region with an infinitely long n^+ substrate is

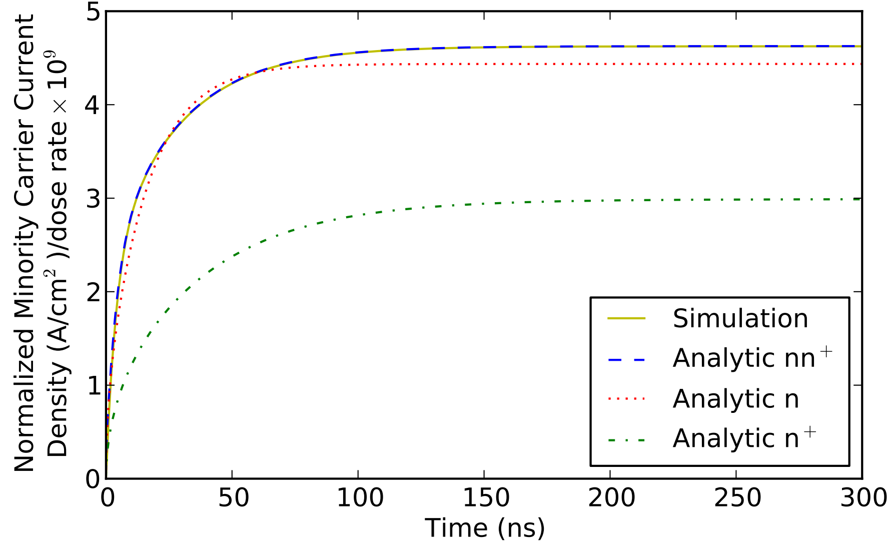

Figure 5: The transient normalized analytic and TCAD photocurrent densities for nn^+, n^+ and n regions for a long 1×10^9 rad(Si)/s dose-rate irradiation.

5.4875 A/cm^2. This was computed with equation (20) by replacing A with the A_∞ of equation (B-5), which is shown in Appendix B to be identical to the steady-state photocurrent solution of [3]. In steady-state (after 1×10^{-4} s), the TCAD simulations yield a photocurrent of 5.4978 A/cm^2 for the 100 μm thick n^+ substrate, and 5.4830 A/cm^2 for the 30 μm thick substrate.

3.1.2 TCAD and Analytic Comparisons for a Short Radiation Pulse

An important property of our analytic solution is that it is accurate for both short and long radiation pulses, when compared to TCAD simulations. For this reason, we demonstrate in this section that the analytic photocurrent solution presented in the previous section for a long current pulse also agrees well with the TCAD solution for a short current pulse. Figure 7 shows the analytic and TCAD normalized minority carrier photocurrent response for the nn^+ doped silicon region of the ideal diode due to a 1 ns pulse at various radiation levels. We again see that the analytic model is in very close agreement to the TCAD model for low to mid-level irradiation conditions. For very high irradiations, the peak photocurrent increases by a small amount, and there is a slight bulge in the tail; but the use of the analytic solution for high-level irradiations in this case does not produce an unacceptable error for most applications.

3.1.3 Numerical and Analytic Comparisons for a pnn^+ Epitaxial Diode

Figure 8 illustrates the normalized total and undepleted region minority carrier photocurrent densities for a long 1×10^9 rad(Si)/s dose rate radiation pulse irradiating the model pnn^+ epitaxial diode. Both the analytic solution and TCAD simulations performed by the Sentaurus simulator

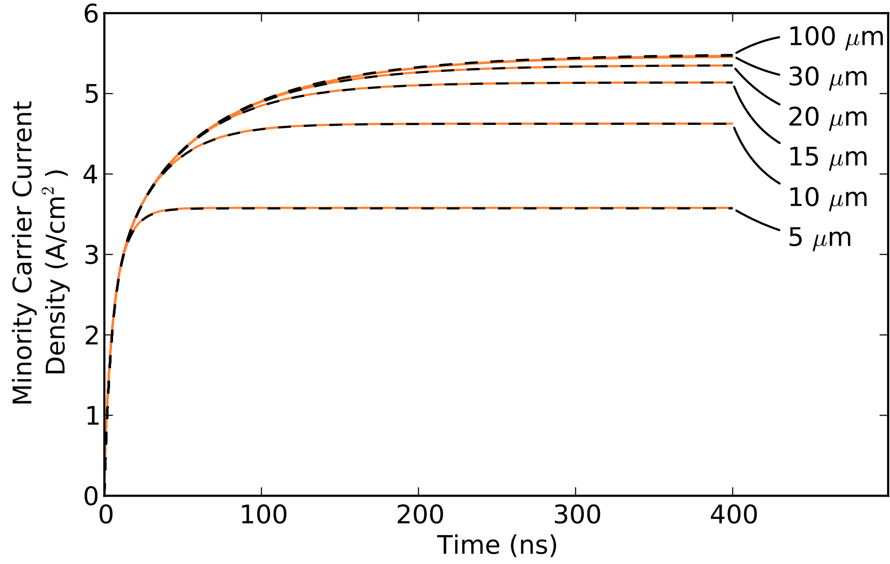

Figure 6: The transient normalized analytic and TCAD photocurrent densities for the nn^+ region as a function of the substrate width, $w_2 - w_1$, for a long 1×10^9 rad(Si)/s dose rate irradiation.

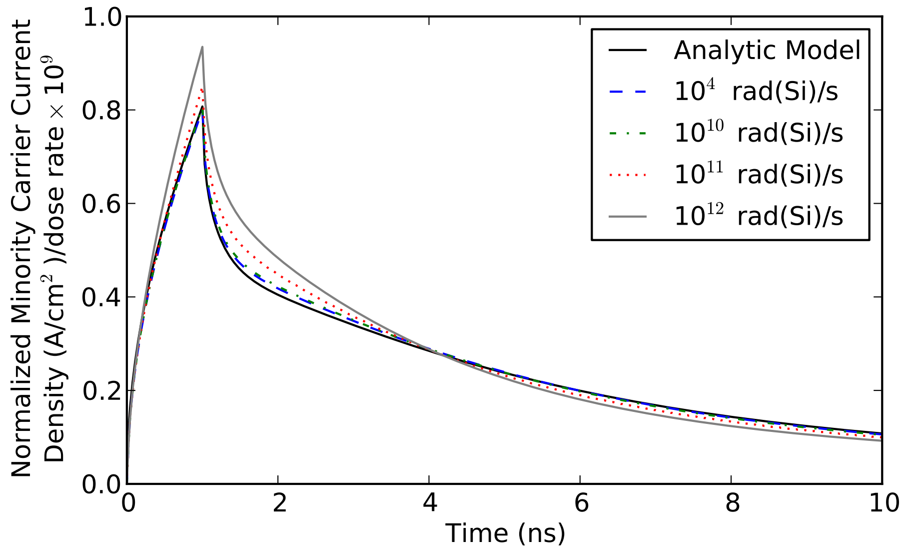

Figure 7: The normalized TCAD and analytic transient photocurrent densities for the nn^+ region for a 1 ns, 1×10^9 rad(Si)/s dose irradiation. The dose rates for Sentaurus irradiations are given in the legend.

are shown. The TCAD normalized photocurrent densities, given by dashed lines in the figure, are computed by the Sentaurus code assuming a 5 V reverse bias and the parameters of Table 2. The total analytic normalized minority carrier photocurrent is computed using equation (5), assuming the previously-computed nn^+ photocurrent (J_{pp}) and the undepleted p region photocurrent (J_n) calculated using the photocurrent solution of [16]. The analytic depletion current, $J_{depl} = qg(t)W$, is calculated with W computed from the pn depletion approximation using the base and collector

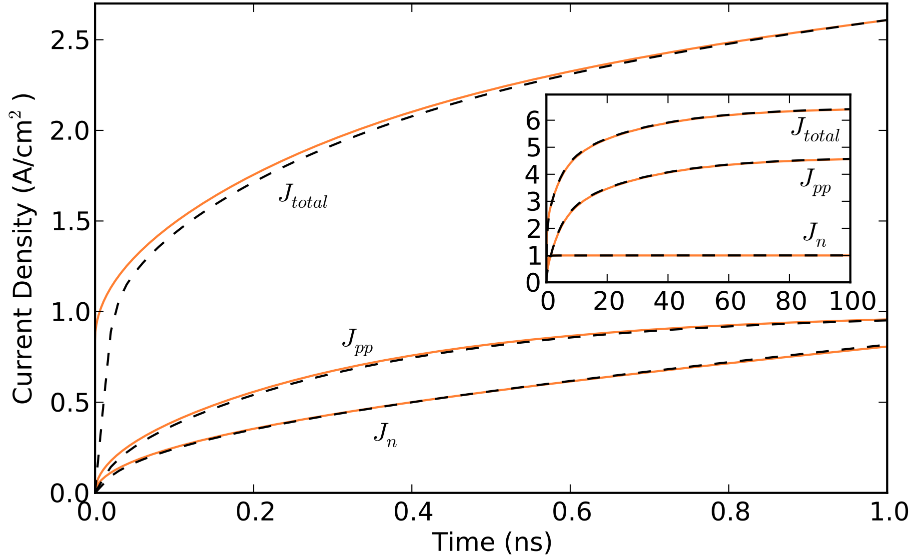

Figure 8: Short and long time scale transient normalized TCAD and analytic transient photocurrent densities for the pnn^+ diode for a 1×10^9 rad(Si)/s dose rate radiation pulse. The inset shows the photocurrents over a longer time scale.

parameters and an applied bias of -5 V.

It is apparent from the plot that the TCAD and analytic photocurrents are very close for $t > 0.2$ ns. At very early times, $t \leq 0.1$ ns, the analytic solution overestimates the TCAD result for total photocurrent. The most likely explanation is the simple model used to compute the photocurrent from the depletion zone. Obviously, there is some recombination of carriers in the depletion region and the collection of these carriers is not instantaneous in the TCAD model.

3.2 Comparison for a Realistic Epitaxial Device, the 2N2222 Transistor

In this section, we compare the analytic, TCAD, and Xyce-computed photocurrent and excess carrier densities for simplified 1D versions of the 2N2222 transistor (herein called the 2222). A detailed description of the transistor can be found in [23]. We evaluate the effect of circuit elements, as well as the inert zero-biased emitter part of a circuit on the photocurrent. The focus is to evaluate the error between the TCAD and analytic simulations as we approach a more complex TCAD/circuit model. Also of interest is to demonstrate when, and if, the new analytic model is superior to the compact photocurrent model [2] presently used in Xyce.

We compare results using two generation function waveforms. The first is a step wave pulse with a dose rate of 5.8×10^8 rad(Si)/s. The step wave simulations were used to determine the depletion width during the simulations, as well as the excess minority carrier densities and electric field in the base-collector region. The second waveform is a sawtooth generation function waveform, shown in Figure 9. The maximum of this waveform corresponds to the peak dose rate of the square wave, and the shape was selected in order to compare the time-dependence of the various models. The

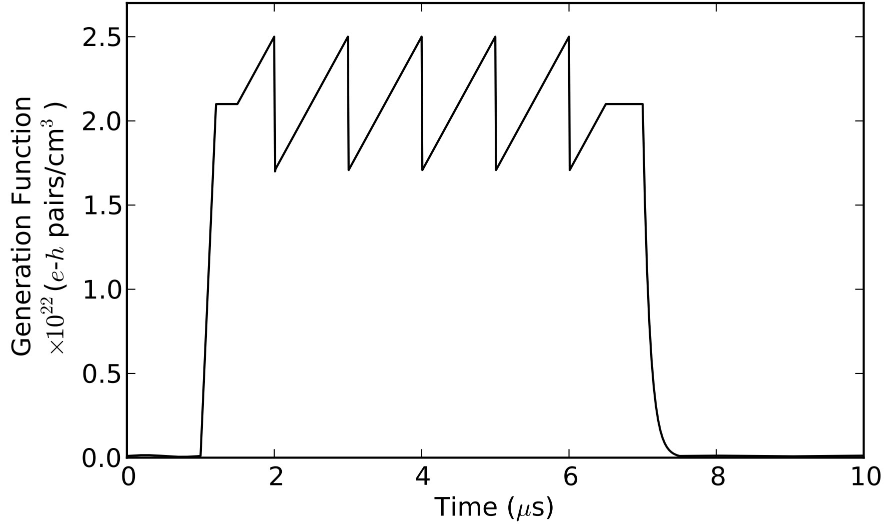

Figure 9: Sawtooth generation function used for comparison of TCAD, analytic and Xyce codes.

purpose of the sawtooth waveform comparison is to evaluate the differences between the analytic and the Xyce photocurrent models for the same calibrated set of parameters. Additionally, we compare the TCAD and analytic models for the same waveform at higher and lower frequencies (short and long pulses) to evaluate the robustness of the analytic model. The high and low frequency pulses are obtained by using the same pulse amplitude, but scaling the time by a multiplicative factor. We also compare the analytic and TCAD models at two biases: -5 V and -10 V.

The analytic photocurrent model is capable of simulating a pnn^+ device with uniform doping, but cannot take into account a doping profile or spatially-dependent mobilities or lifetimes. As such, the doping profiles associated with the real device are replaced with abrupt junctions and uniform doping. Table 3 gives the doping, mobility, lifetime and width for each diode region used in the analytic and TCAD models of the 2222 device. Only the minority carrier parameters are used in the analytic model. For the TCAD simulations, the majority carrier lifetimes are set to the values of the minority carrier lifetimes. Some experimentation with the majority carrier lifetimes using the TCAD models indicated that their effect on the photocurrent was minimal. The doping values in the collector and sub-collector correspond approximately to the measured doping concentrations in the areas where the doping is constant (see Figure 4.1 of [23]), that is, the values in the regions outside of the transition zones. The values of the minority carrier mobility and lifetime used in the analytic and TCAD models were obtained through calibration of the Xyce model to photocurrent data [23] taken at the timescale of the pulse shown in Figure 9. Table 4 lists the widths of the various regions used in the analytic model, which were calculated from the Sentaurus simulation results.

For the analytic model, the photocurrent from the diode is computed as the sum of the photocurrents computed by solving the ADE in each of the undepleted regions, and adding in the current from the well depletion zone. In the analysis of Section 3.1, the undepleted region solutions for the transient cases were calculated with the equations presented in Section 2.2. However, the genera-

Table 3: 2222 physical parameters. Only the minority carrier parameters are used in the analytic model.

Region	μ_n **(cm^2/V·s)**	μ_p **(cm^2/V·s)**	τ_n, τ_p **(s)**	**Doping (cm^{-3})**	**Width (μm)**
emitter (n)	1161	77.4	2.0×10^{-8}	4.0×10^{19}	2.0
base (p)	638.3	127	4.0×10^{-8}	2.0×10^{16}	1.6
collector (n)	3191	445	2.0×10^{-6}	6.0×10^{14}	4.52
sub-collector (n^+)	2553	511	2.0×10^{-7}	1.0×10^{18}	200.

Table 4: 2222 widths used in the analytic model in μm. The sub-collector had a width of 200 μm in all of the simulations.

Region	**Device simulation**		
	nn^+ **&** pnn^+		$npnn^+$
	5 V	10 V	5 V
undepleted emitter (n)	–	–	2.0
emitter-base depletion	–	–	0.248
undepleted base (p)	1.561	1.526	1.313
base-collector depletion	3.133	4.248	3.133
undepleted collector (n)	1.426	0.346	1.426

tion function in Figure 9 was expressed as a discrete data set, and the solutions from Section 2.2 can not be applied to a waveform that does not have an analytic expression. Therefore, a solution for the case of a general piecewise linear generation function was developed. This solution is shown in Appendix C, with the expression for the analytic photocurrent density being given by Equation (C-7).

In the previous analysis of the excess minority carrier density and photocurrent from an unbiased nn^+ doped diode collector/subcollector region, the analytic solution agreed almost exactly with Sentaurus simulations. The principle differences between that structure and the 2222 structure are that the 2222 has a lower doping concentration in the collector region, and the thickness of the undepleted region of the collector is significantly smaller, especially at the -10 V bias. This results in a significant ohmic field in the collector region in TCAD simulations due to the high resistivity in the lightly n-doped 2222 collector. This electric field is not accounted for in the analytic simulations. In addition, the analytic and TCAD excess minority carrier densities at the collector/-subcollector boundary may also be different due to the proximity of this transition region to the depletion edge in the 2222 structure. Due to these and other possible differences, the calculated photocurrent for the 2222 from the analytic method and TCAD simulations could be significantly different.

3.2.1 Simulations of the nn^+ Region

Figure 10 gives a comparison of the excess minority carrier density concentration in the 1D abrupt junction nn^+ collector and subcollector regions of the 2222 diode, computed using the steady-state analytic model, and numerically with the Medici and Sentaurus codes. Medici [24], like Sentaurus, is a TCAD drift-diffusion code. A square wave generation function and two applied biases were assumed in Figure 10, with the nn^+ collector and subcollector region parameters set according to the data of Tables 3 and 4. The radiation dose rate was 5.8×10^8 rad(Si)/s for all the simulations. To ensure the excess carrier density calculated from the TCAD simulations was from a steady-state condition, the irradiated densities were extracted at the end of a 1×10^{-4} second pulse. The analytic simulation is the steady-state excess minority carrier density after an infinitely long pulse. The Medici and analytic solutions are for the nn^+ region only, where the widths of the n region at the two biases were computed from the Sentaurus simulations, and are given in Table 4. The Sentaurus solutions include the entire diode, with the bias applied at the base and subcollector contacts. It is apparent from this figure that the proximity of the nn^+ interface to the depletion edge in the 2222 structure significantly lowers the excess minority carrier density in the collector as compared to the analytically-computed excess carrier density. Similarly, from the Sentaurus simulation of the entire diode structure, we see that the conditions for the idealized zero excess minority carrier boundary condition at the depletion edge are not met, particularly at the higher bias.

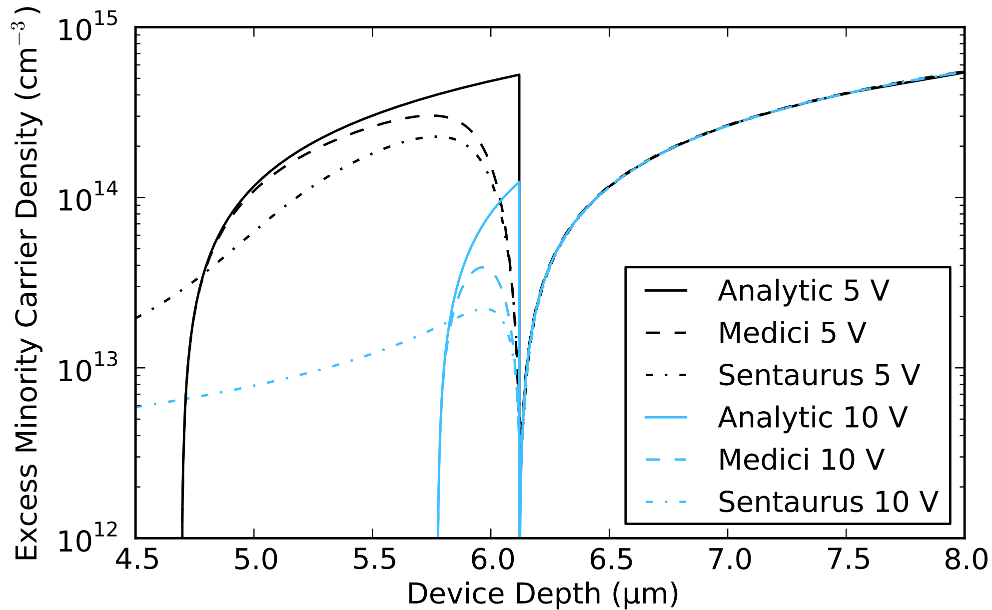

Figure 10: Comparison of excess minority carrier densities in the 1D abrupt junction nn^+ collector and subcollector regions of the 2222 diode at steady-state, due to an infinite 5.8×10^8 rad(Si)/s irradiation pulse. The Medici results simulate only the nn^+ collector and subcollector regions and the Sentaurus results are for the entire pnn^+ diode. The reverse biases applied across the base and sub-collector are indicated.

Figure 11 gives the 2222 collector region electric fields, as computed by the Sentaurus program

with no irradiation. The entire pnn^+ diode is simulated. We observe clear, separate pn and nn^+ depletion regions in this figure at 0 V and -5 V biases, with only a small field in the undepleted collector at -5 V. A significant electric field occurs throughout the collector region of the device at -10 V. This indicates the pn and nn^+ depletion zones are not fully distinct in this case, which is reflected in the sub-micron width of the undepleted n region shown in Table 4 for the -10 V bias condition.

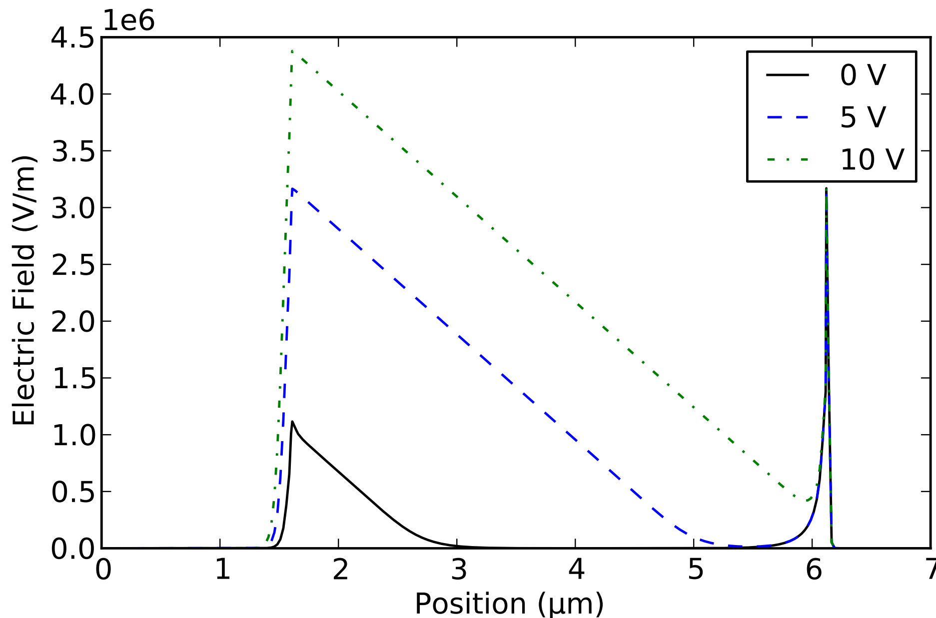

Figure 11: The numerically-computed electric field in the 1D abrupt junction nn^+ collector and subcollector regions of the 2222 diode for 0 V, -5 V, and -10 V biases, as calculated by Sentaurus with no irradiation.

From the plots in Figures 10 and 11, one might expect a significant difference between the analytic and TCAD nn^+ minority carrier photocurrents generated with the generation function given by Figure 9. The results of a Sentaurus simulation of just the nn^+ region, along with the analytic result using the undepleted regions widths given above, are shown in Figure 12. As seen in the figure, there is very little difference between the two photocurrent densities. This result could be surprising, since there are significant differences in the excess carrier density inside the collector, and the idealized boundary condition between the n and n^+ regions is not met in the TCAD simulations. The explanation comes from the fact that the current flux leaving the nn^+ region is defined by the derivative of the excess carrier density at the boundary with the depletion region (see equation (22)). As can be seen in Figure 10 for the steady-state case, the analytic solutions overlap the Medici simulations (which include only the nn^+ regions) at the depletion region boundaries. It would appear that the error produced by the boundary condition for the nn^+ interface does not appreciably affect the solution at the boundary with the depletion region. Since the derivatives are nearly equal, so are the current densities. Even though Figure 10 reflects the steady-state case, the same explanation would apply for the dynamic case of Figure 12. The reasons for this are explored next.

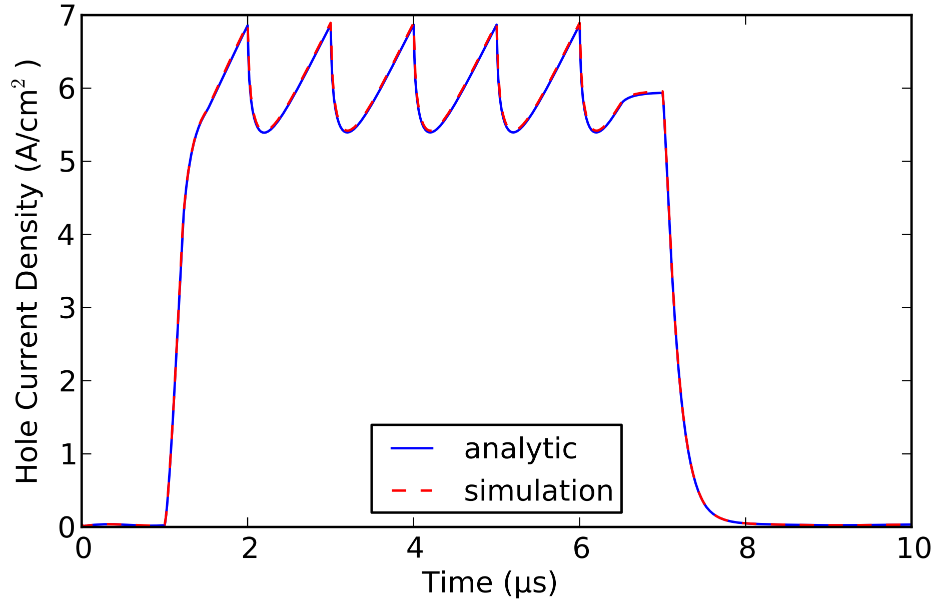

Figure 12: Comparison of the minority carrier photocurrent density from the 1D abrupt junction nn^+ collector and subcollector regions of the 2222 diode. The TCAD results are from the Sentaurus simulations of the nn^+ region of zero-biased 2222 diode, assuming the undepleted collector width computed by applying a bias of -5 V on the entire diode.

The generation function given in Figure 9 is effectively a long, low frequency pulse, so the photocurrent response at any point along the curve is almost entirely described by the steady-state photocurrent. We note that by scaling the generation function with respect to time (dividing by 100, e.g.), we produce a short pulse with high frequency components. In this case one might not expect the conditions present in the steady-state solution to apply. Figure 13 compares the analytic model with the Sentaurus TCAD simulation for a pulse compressed by a factor of 100. Surprisingly, we again find that the analytic and TCAD photocurrents are essentially the same, though the overall shape of this photocurrent curve has changed significantly from the low-frequency comparison. This indicates a robustness of the analytic model's ability to faithfully reproduce the excess carrier density (and, thus, the current density) at the boundary of the nn^+ region with the depletion zone, even outside the steady-state condition.

3.2.2 Simulations of the Full 2N2222 Transistor and the pnn^+ Region

In this section, we compare simulations of the 2222 photocurrent from the Sentaurus TCAD model, the analytic model, and the Xyce circuit code. Special attention will be given to the pnn^+ diode component of the transistor. Reverse biases of 5 V and 10 V are considered, as well as responses to modified versions of the generation function given by Figure 9, where the time parameter is either compressed or expanded. For these simulations there are some differences between the models that cannot be controlled; for example, the excess minority carrier density at the edge of the depletion zone is assumed to be zero in the analytic model, whereas this is not in the case in the TCAD

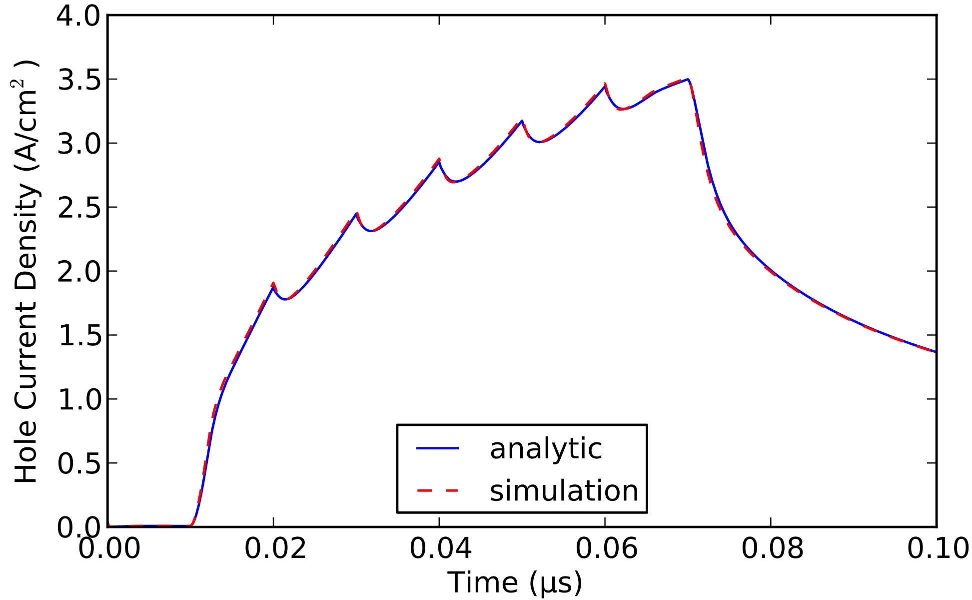

Figure 13: Comparison of the minority carrier photocurrent density from the 1D abrupt junction nn^+ collector and subcollector regions of the 2222 diode where the time scale of the generation function of Figure 9 has been divided by 100. The TCAD results are from the Sentaurus simulations of the nn^+ region of the zero-biased 2222 diode, assuming the undepleted collector width computed by applying a bias of -5 V on the entire diode.

simulations, as shown by the Sentaurus plots in Figure 10. Likewise, in the TCAD simulation the depletion zone boundary is not abrupt.

The Xyce simulations and some of the Sentaurus simulations included a circuit model that represented one used to test the 2222 bipolar junction transistor (BJT) at radiation facilities. Figure 14 shows the BJT as a circuit element within the testing circuit. The bias is applied through a voltage source located at the bottom right node in the figure. The purpose of the low-pass RC circuit at the right side of the BJT is to reduce a possible voltage drop at the power source due to the limited response time of real power sources; the charge in the large capacitor helps to maintain a constant potential at the sub-collector. The 50 Ω resistor at the base of the BJT allows the measurement of the photocurrent, which is computed from the voltage drop across the resistor. The emitter is tied to the base contact to maintain zero potential across this junction. Sentaurus simulations with and without the external circuit had nearly identical responses for all but the highest frequency simulations.

In order to compute the photocurrent from the analytic model for the full 2222 device, the emitter must be added to the pnn^+ device. We assume the bias across the emitter and base to be 0 V, although the bias can vary in the actual circuit. Since the doping in the emitter is three orders of magnitude greater than the base, we compute the width of the resulting np emitter-base depletion region using the one-sided junction approximation (formula 6.22 in [25]), and assume that the entire depletion region is in the base. Our analytic photocurrent computation is thus modified by

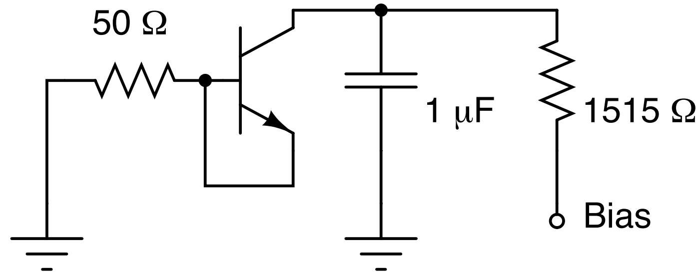

Figure 14: 2N2222 BJT and the circuit used in radiation testing and in the Xyce simulations. The voltage induced by the photocurrent is measured at the node between the 50 Ω resistor and the BJT base.

adding the photocurrent collected from the emitter-base depletion zone and the entire undepleted emitter. We also modify the width of the undepleted base by subtracting from it the emitter-base depletion zone width. The widths are given in Table 4, and the other parameters are in Table 3.

The mobility and lifetime parameters used in the calibration of the Xyce model of the 2222 are taken from [23], and do not match those associated with these doping levels in most publications. The values were obtained by calibration of the Fjeldly model [2] with data from 2222 radiation tests. These parameters were used in the analytic simulation, but doping parameters from Figure 4.1 of [23] were used to establish the boundary condition at the nn^+ interface. The same parameters were also used in the Sentaurus model, and are shown in Table 3.

Figure 15 gives the comparison between the three models for the nominal generation function (shown in Figure 9). Subfigure 15a includes the full transistor as it behaves in the circuit of Figure 14, while Subfigures 15b and 15c include only the reverse-biased pnn^+ diode part of the 2222. The good agreement between the Sentaurus, analytical, and Xyce simulations is in part due to the fact that the radiation pulse is long and changes slowly with respect to time, so that the photocurrent is dominated by the steady-state photocurrent from the nn^+ region. This is likely part of the reason that the Xyce solution is in agreement with the analytic and TCAD results, since the Fjeldly [2] model utilizes the same steady-state solution as the analytic model. From the graph we note that the Xyce response to changes in the generation function is a bit slower than that of the analytic model.

We next compare the three models for the case where the time in Figure 9 is compressed by a factor of 100, similar to the comparison shown in Figure 13 in the previous section. Figure 16 gives the comparison in this case. Good agreement between the Sentaurus and analytical simulated photocurrents is apparent, but the Xyce simulation shows a significant drop in the current with respect to the other two models. In this case the photocurrent is no longer determined by the steady-state solution and is not dominated by the nn^+ region, since carriers from deep within this region have not had time to diffuse to the nn^+ boundary. From the graph we note a marked improvement in using the analytic photocurrent model over the model employed in Xyce. The initial differences between the analytic model and Sentaurus are likely due to the violation of the boundary condition at the depletion zone and the simple analytic model employed to compute the depletion zone photocurrent.

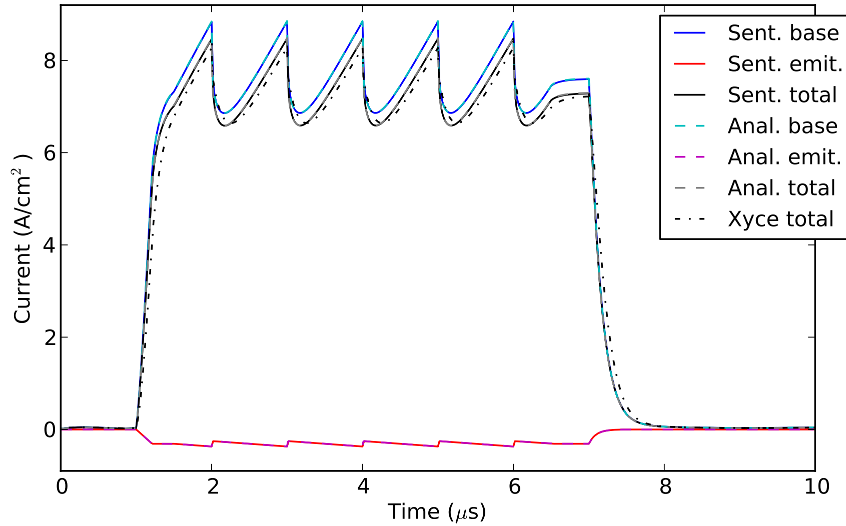

(a) Full transistor and circuit with a 5 V bias

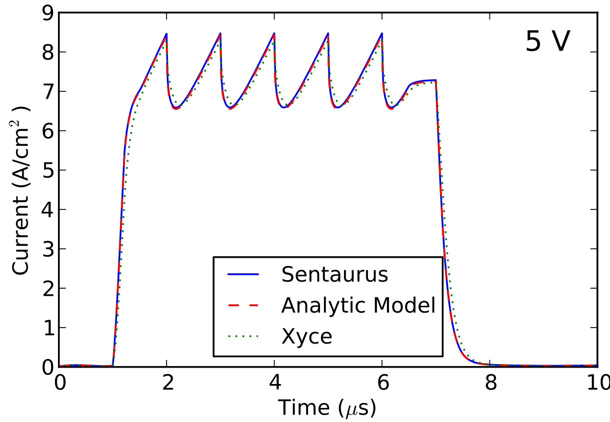

(b) pnn^+ region with a 5 V bias

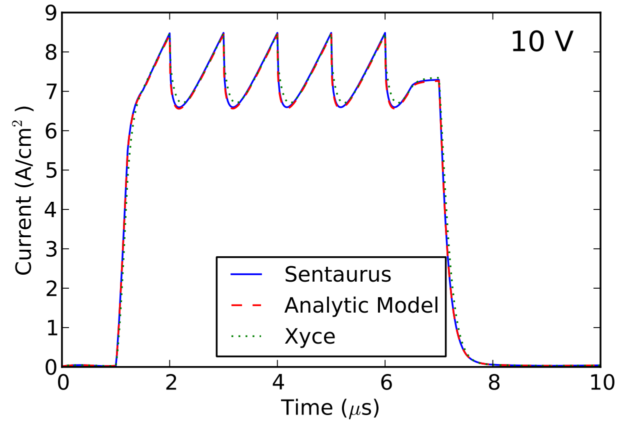

(c) pnn^+ region with a 10 V bias

Figure 15: Comparison of the photocurrent density from the 2222 computed using the Sentaurus TCAD simulator, the analytic code, and the Xyce circuit simulator for the generation function given in Figure 9.

We now compare the three models for the case where the time in Figure 9 is compressed by a factor of 1000, which is shown in Figure 17. For this very short waveform, the agreement between the Sentaurus and analytical simulated photocurrents is not quite as good, but within a factor of 20% for both the 5 V and 10 V biases. The photocurrent with both the Sentaurus and analytic simulations increases with time in a similar manner, reflecting increasing charge collection from the n^+ substrate. For the 5 V bias, the Xyce simulation peaks at less than 50% of the Sentaurus peak, and does not increase significantly with time, since it is not based on a physical model in which the percentage of charge collected may increase with time. For this short pulse, the photocurrent is dominated by the depletion and n collector regions, and, as noted in the nn^+ subsection, there are significant differences between the TCAD and analytical excess carrier distributions in these regions. Nevertheless, the analytic model demonstrates a significant improvement over the Fjeldly

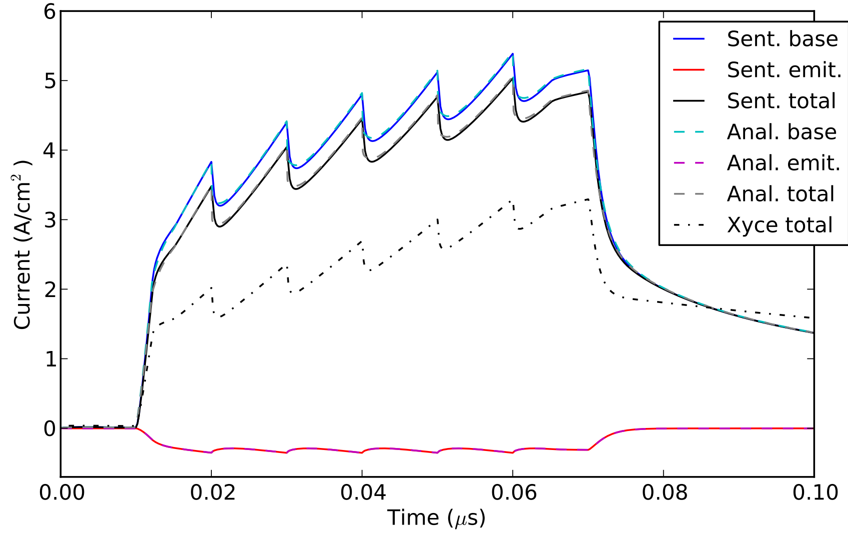

(a) Full circuit with a 5 V bias

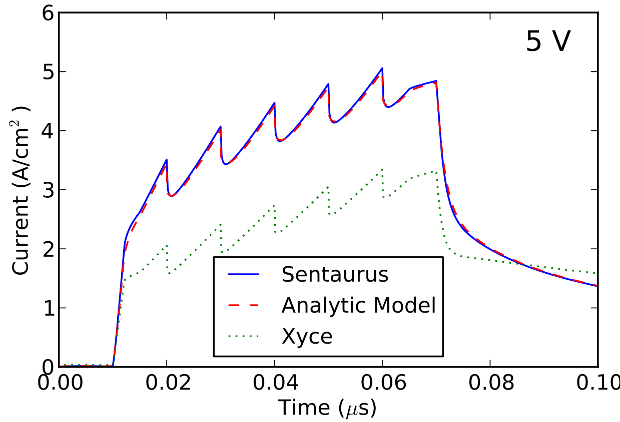

(b) pnn^+ region only with a 5 V bias

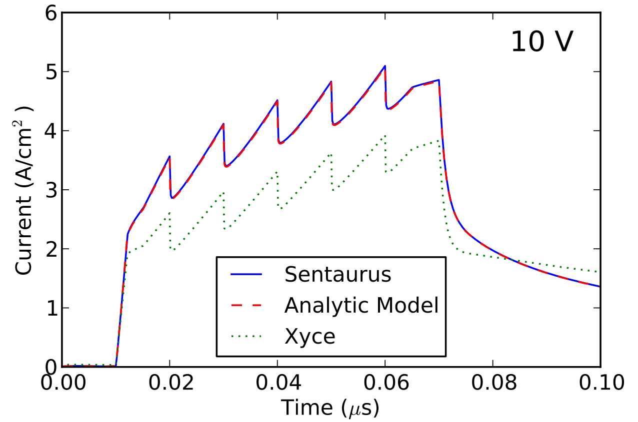

(c) pnn^+ region only with a 10 V bias

Figure 16: Comparison of the photocurrent density from the 2222 computed using the Sentaurus TCAD simulator, the analytic code, and the Xyce circuit simulator for the generation function given in Figure 9, time-compressed by a factor of 100.

model employed in Xyce.

Finally, we compare the three models for the case where the time in Figure 9 is expanded by a factor of 10. This low-frequency generation function tests the steady-state photocurrent feature of the three models. The photocurrent for the analytic and Sentaurus models is dominated by the minority carrier photocurrent from the nn^+ region. We would expect that the Xyce model would also give accurate results for this generation function because it uses an exact steady-state diffusion model. Figure 18 gives the comparison in this case, and we observe that all models predict the same photocurrent and that this photocurrent has the same shape as the input generation function.

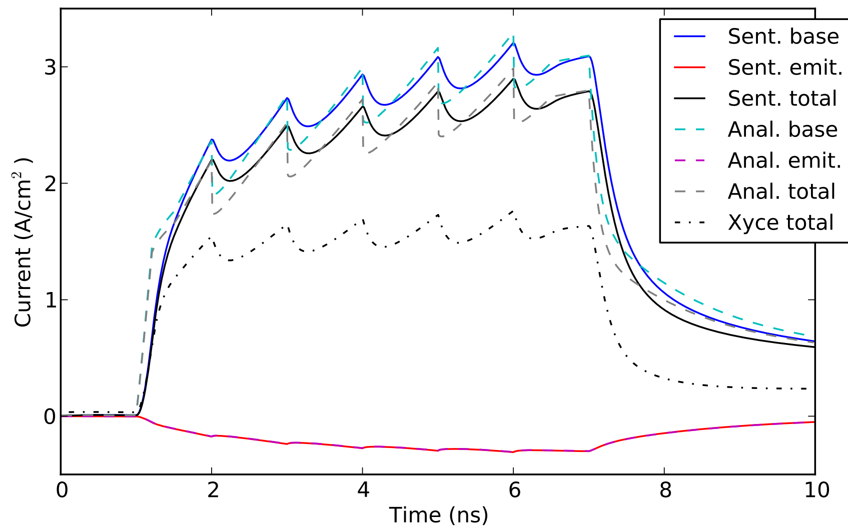

(a) Full circuit with a 5 V bias

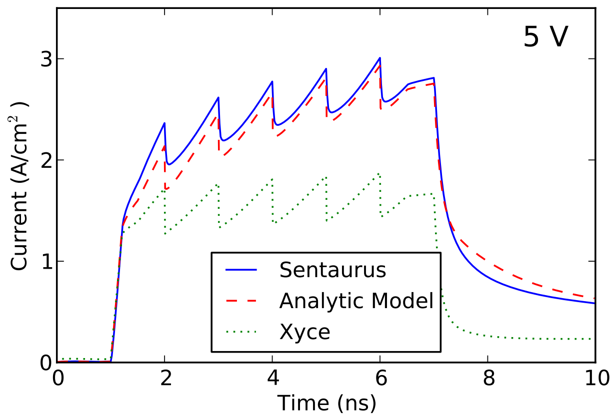

(b) pnn^+ region only with a 5 V bias

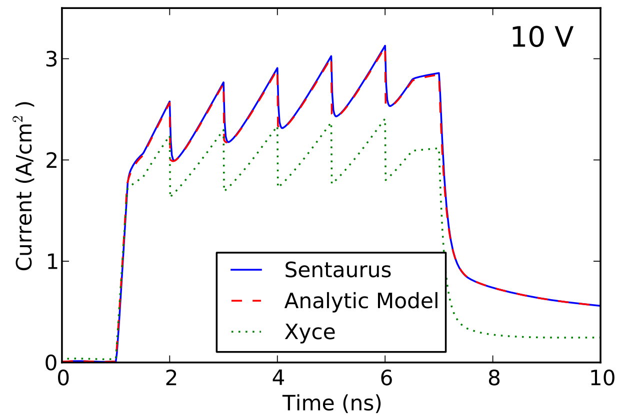

(c) pnn^+ region only with a 10 V bias

Figure 17: Comparison of the photocurrent density from the 2222 computed using the Sentaurus TCAD simulator, the analytic code, and the Xyce circuit simulator for the generation function given in Figure 9, time-compressed by a factor of 1000.

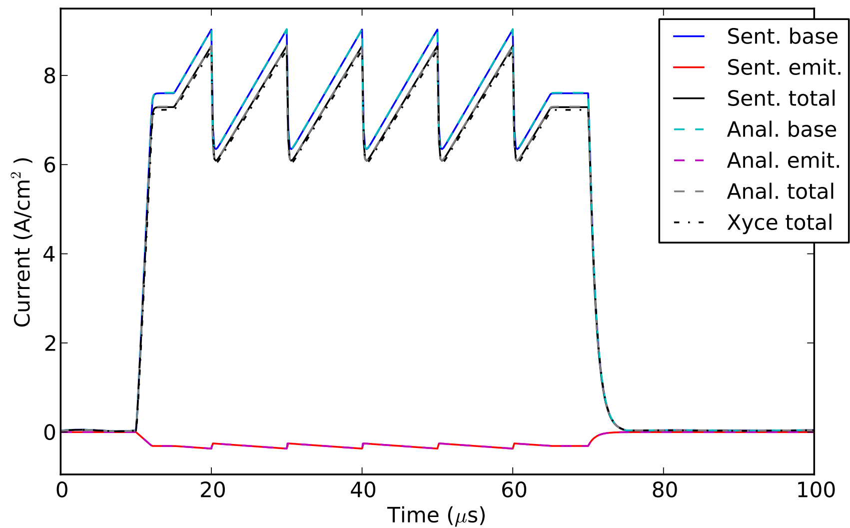

(a) Full circuit with a 5 V bias

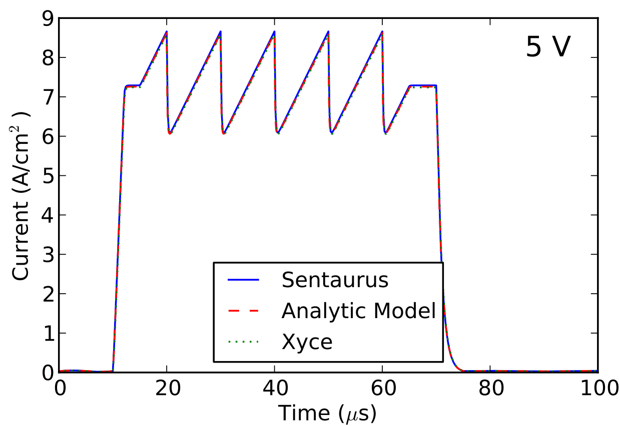

(b) pnn^+ region only with a 5 V bias

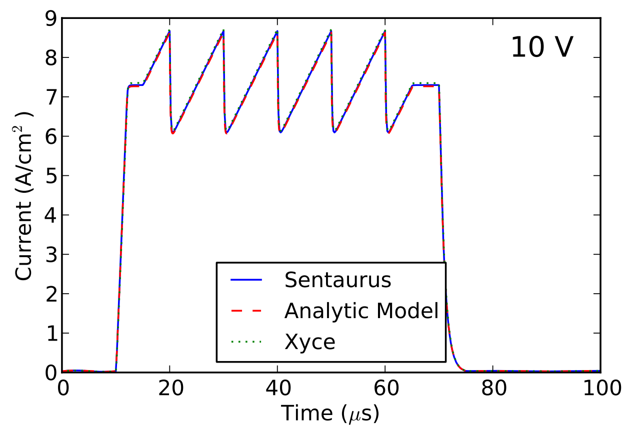

(c) pnn^+ region only with a 10 V bias

Figure 18: Comparison of the photocurrent density from the 2222 computed using the Sentaurus TCAD simulator, the analytic code, and the Xyce circuit simulator for the generation function given in Figure 9, time-expanded by a factor of 10.

4 Conclusions

We presented a new analytic solution that determines the excess minority carrier density in an irradiated finite 1D reverse-biased pnn^+ abrupt junction epitaxial diode. The solution was developed by solving the ambipolar diffusion equation (ADE) for the excess carrier concentrations in the undepleted nn^+ region of a device using the finite Fourier transform technique. The use of finite Fourier transforms to solve photocurrent problems was originally presented in reference [16] for a device that did not include a subcollector.

For the present work, the ADE was adapted to include an n^+ sub-collector region, and an epitaxial-subcollector interface at the nn^+ boundary. Boundary conditions, consistent with ohmic contacts and current continuity at the epitaxial interface, were imposed to obtain the minority carrier density from this region. An additional boundary condition, first suggested in reference [3], was used to relate the excess carrier densities on either side of the (n-n^+) interface. The resulting ADE for the nn^+ region was then solved for both the steady-state and transient cases.

The analytic excess minority carrier and photocurrent density solutions in the nn^+ region are composed of a closed-form steady-state term, and a transient term presented in the form of an infinite series. The BVP from which these solutions were derived was solved using the finite Fourier transform technique. The required eigenvalues and eigenfunctions were obtained by applying separation of variables to the corresponding homogeneous BVP, leading to a composite Sturm-Liouville problem. The form of the eigenfunctions depended upon the device parameters, as did the eigenvalues, which were determined by the zeros of a transcendental equation. Our steady-state photocurrent solution was shown to approach other steady-state photocurrent solutions [3], [4] when the appropriate limits were applied.

The analytic solution was compared to TCAD device simulations for both an ideal and a realistic device. The ideal device was a pnn^+ diode, devised so that many of the assumptions inherent to the analytic model—but not necessary for TCAD—were true. The purpose of this comparison was to verify the validity of the analytic solution within the confines of its assumptions. The device chosen for the realistic (non-ideal) case was a 2N2222 bipolar junction transistor (BJT). For this case, comparisons were made to the Xyce circuit simulator in addition to TCAD. Xyce implements the Fjeldly [2] model for photocurrent. The purpose of this comparison was to show how applicable the new analytic solution could be for a realistic scenario, and also demonstrate its superiority over previous, less mathematical, compact models for photocurrent.

In the ideal pnn^+ diode case, comparison between TCAD simulations and the analytic excess carrier density solutions of only the nn^+ region of the diode, when it was irradiated and unbiased, showed excellent agreement at low-level dose rates (less than 1×10^{10} rad(Si)/s) for both short and long radiation pulses. In particular, the discontinuity at the nn^+ interface was reproduced in the TCAD simulations, giving credence to the use of the analytic solution boundary conditions shown in equations (10) and (11). At levels of irradiation up to 1×10^{10} rad(Si)/s, the comparison showed that the analytic photocurrent solution gives an acceptable approximation to the TCAD model if the parameters are kept consistent. Additional nn^+ region photocurrent simulations as a function of increasing substrate width for a long-duration 1×10^9 rad(Si)/s radiation pulse also showed

superb agreement between the TCAD and analytic solutions. The excellent agreement between analytic and TCAD photocurrents for both short and long radiation pulses demonstrated that our analytic model may be used over a wide range of conditions without recalibration for changes in pulse width.

The ideal diode case was extended by examining a complete pnn^+ reverse-biased diode. In this case, the analytic photocurrent solution requires the addition of the *p* and depletion region components. Assuming a simple depletion current model, the analytic solution of [16], and approximating the width of the depletion region in the analytic solution from the *pn* diode approximation, we again showed excellent agreement between the TCAD and analytic photocurrents for the model case (less than 0.2% error for $t > 0.4$ ns).

For the non-ideal case of the 2222 BJT, the analytic model, again, had excellent performance when compared with the TCAD and Xyce codes. The collector (*n*-type) region of the 2222 had a much lower doping level than in the idealized model case, the result being a much larger depletion region. In fact, for a -10 V bias on the base-collector diode, the *pn* depletion region began to merge with the small depletion zone around the nn^+ interface. Therefore, while the steady-state excess minority carrier density calculated from the analytic model agreed well with the TCAD simulation for the unbiased case, the agreement was not as good for the biased cases. Nevertheless, photocurrents from the nn^+ regions calculated for transient sawtooth radiation pulses with varying frequencies had excellent agreement.

In addition to the nn^+ region, results from the pnn^+ region and full 2222 transistor were also examined. The response of the transistor in a tester circuit was simulated using both the TCAD and Xyce codes. For a sawtooth pulse 6 μs in duration, all three codes showed nearly identical predictions for the photocurrent. However, when the pulse was shortened to 60 ns, Xyce significantly underpredicted photocurrent compared to the other two methods. The difference was even more severe for a 6 ns pulse. In this case, the analytic model also deviated slightly from the TCAD simulation. Nevertheless, the agreement was still much superior to the Fjeldly model used by Xyce. Finally, in the near steady-state case of a 60 μs pulse, all three codes were essentially indistinguishable.

While the analytic model had an excellent match to almost all the TCAD simulations presented in this report, it is possible that several factors could contribute to less accurate results for other devices, as follows. First, we approximate the depletion width (W) used in the analytic computation of J_{depl} utilizing the analytic formula for an abrupt *pn* junction diode. The depletion width for a pnn^+ junction diode is affected by the nn^+ interface. Second, there is not an abrupt depletion boundary in real devices. Despite issues with the depletion region approximation, they are not significant for all devices, and for devices in which they are significant, it should be possible to mitigate them with judicious use of calibration.

In summary, our analytic model showed excellent agreement with a commercial TCAD code for the prediction of photocurrent in pnn^+ diode structures. In the cases examined in this report, the agreement was better than the Fjeldly [2] model currently used by Xyce. Though expected to be slightly more computationally expensive than the Fjeldly model, we anticipate our analytic model to be a superior solution for the fast and accurate calculation of photocurrent, and thus could be the basis for an improved compact model for photocurrent.

References

[1] L. W. Nagel. Spice2: A computer program to simulate semiconductor circuits. *ERL Memo*, (ERL-M5250), May 1975.

[2] T. A. Fjeldly, Y. Q. Deng, M. S. Shur, H. P. Hjalmarson, A. Muyshondt, and T. Ytterdal. Modeling of high-dose-rate transient ionizing radiation effects in bipolar devices. *IEEE Transactions on Nuclear Science*, 48(5):1721–1730, 2001.

[3] D. M. Long, J. R. Florian, and R. H. Casey. Transient response model for epitaxial transistors. *IEEE Transactions on Nuclear Science*, NS-30(6):4131–4134, 1983.

[4] O. M. Stuetzer. Extended steady-state analysis of the gamma-irradiated cartesian p-n junction. Technical Report SAND86-7174, Sandia National Laboratories, Albuquerque, NM, 1987.

[5] Eric R. Keiter, Thomas V. Russo, Eric L. Rankin, Richard L. Schiek, Heidi K. Thornquist, Deborah A. Fixel, Todd S. Coffey, Roger P. Pawlowski, Keith R. Santarelli, and Christina E. Warrender. Xyce parallel electronic simulator: User's guide, version 5.2. Technical Report SAND2011-2515, Sandia National Laboratories, Albuquerque, NM, 2011.

[6] Y. Taur and G. Gildenblat. *Compact Modeling: Principles, Techniques and Applications*. Springer-Verlag, 2010.

[7] *Sentaurus Device User Guide Version E-2010.12*. Mountain View, CA, December 2010.

[8] Gary L. Hennigan, Robert J. Hoekstra, Joseph P. Castro, Deborah A. Fixel, and John N. Shadid. Simulation of neutron radiation damage in silicon semiconductor devices. Technical Report SAND2007-7157, Sandia National Laboratories, Albuquerque, NM, October 2007.

[9] Kartikeya Mayaram and Donald O. Pederson. Coupling algorithms for mixed-level circuit and device simulation. *IEEE Transactions on Computer Aided Design*, II(8):1003–1012, 1992.

[10] S. Selberherr. *Analysis and Simulation of Semiconductor Devices*. Springer-Verlag, New York, 1984.

[11] J. P. McKelvey. *Solid State and Semiconductor Physics*. Malabar, Florida, 1966.

[12] J. L. Wirth and S. C. Rogers. Transient radiation current generator model for semiconductor devices. *IEEE Transactions on Nuclear Science*, NS-11:24–38, 1964.

[13] E. W. Enlow and D. R. Alexander. Photocurrent modeling of modern microcircuit p-n junctions. *IEEE Transactions on Nuclear Science*, NS-35(6):1467–1474, 1988.

[14] M. Becker A. N. Ishaque, J. W. Howard and R. C. Block. An extended ambipolar model: Formulation, analytical investigations and application to photocurrent modeling. *Journal of Applied Physics*, 69(1):307–319, 1991.

[15] T. F. Wunsch and C. L. Axness. Modeling of time-dependent transient radiation response of semiconductor junctions. *IEEE Transactions on Nuclear Science*, 39(6):2158–2169, 1992.

[16] C. L. Axness, B. Kerr, and T. F. Wunsch. Analytic light - or radiation - induced pn junction photocurrent solutions to the multidimensional ambipolar diffusion equation. *Journal of Applied Physics*, 96(5):2646–2655, 2004.

[17] W. van Roosbroeck. The transport of added current carriers in a homogeneous semiconductor. *Phys. Rev.*, 91:282–289, Jul 1953.

[18] Carl L. Axness, Bert Kerr, and Eric R. Keiter. Analytic 1D *pn* junction diode photocurrent solutions following ionizing radiation and including time-dependent changes in the carrier lifetime. Technical Report SAND2010-3284, Sandia National Laboratories, 2010.

[19] Carl L. Axness, Bert Kerr, and Eric R. Keiter. Analytic 1-D *pn* junction diode photocurrent solutions following ionizing radiation and including time-dependent changes in the carrier lifetime from a nonconcurrent neutron pulse. *Nuclear Science, IEEE Transactions on*, 57(6):3314 – 3321, 2010.

[20] A. T. Bryant, P. R. Palmer, E. Santi, and J. L. Hudgins. A compact diode model for the simulation of fast power diodes including the effects of avalanche and carrier lifetime zoning. In *Power Electronics Specialists Conference, 2005. PESC '05. IEEE 36th*, pages 2042 –2048, June 2005.

[21] M. N. Özişik. *Boundary Value Problems of Heat Conduction*. International Textbook, Scranton, PA, 1968.

[22] S. M. Sze. *Physics of Semiconductor Devices*. John Wiley and Sons, New York, 1981.

[23] C. E. Hembree, K. E. Kambour, and B. S. Paskaleva. Calibration of Xyce photocurrent models for the QASPR complex prototype circuit. Technical Report SAND2010-4094, Sandia National Laboratories, Albuquerque, NM, 2010.

[24] *TAURUS MEDICI User's Guide*. Synopsys, 2006.

[25] A. S. Grove. *Physics and Technology of Semiconductor Devices*. John Wiley and Sons, Inc., 1967.

A Transient Excess Carrier and Photocurrent Solution Development

In order to obtain the required eigenfunctions and eigenvalues for the finite Fourier transform pair we begin with the (basic) separation of variables process, assuming a solution of the form $u(x,t) = X(x)T(t)$ in the corresponding homogenous versions of equations (6) and (7). The associated composite Sturm–Liouville problem (SLP) consists of the D.E.:

$$\begin{aligned} &D_1X'' - \tfrac{1}{\tau_1}X = -\lambda X \quad , \quad 0 \le x \le w_1 \\ &D_2X'' - \tfrac{1}{\tau_2}X = -\lambda X \quad , \quad w_1 < x \le w_2 \end{aligned} \tag{A-1}$$

in conjunction with the boundary conditions:

$$X(0) = 0 \tag{A-2}$$

$$X(w_2) = 0 \tag{A-3}$$

$$D_1X'(w_1^-) = D_2X'(w_1^+) \tag{A-4}$$

$$N_1X(w_1^-) = N_2X(w_1^+) \tag{A-5}$$

Note, for the corresponding $T(t) = Ce^{-\lambda t}$ component in the product solution(s) to decay equally in both regions, the eigenvalue λ must be the same in both regions, and $\lambda > 0$. The two respective characteristic equations for our SLP are

$$\begin{aligned} &r^2 + \left[\tfrac{\lambda}{D_1} - \tfrac{1}{D_1\tau_1}\right] = 0 \quad , \quad 0 \le x \le w_1 \\ &r^2 + \left[\tfrac{\lambda}{D_2} - \tfrac{1}{D_2\tau_2}\right] = 0 \quad , \quad w_1 < x \le w_2 \end{aligned} \tag{A-6}$$

Considering the three relevant intervals, we know that if $\lambda \le \min\{\frac{1}{\tau_1}, \frac{1}{\tau_2}\}$ both sets of roots are real, and in this case it can be shown that there are no eigenvalues. Conversely, for $\lambda > \max\{\frac{1}{\tau_1}, \frac{1}{\tau_2}\}$, both sets of roots are complex and there are an infinite sequence of eigenvalues, which may be found by expressing the general solution in the form:

$$\begin{aligned} &X = A_1 \sin(\gamma_1 x) \quad , \quad 0 \le x \le w_1 \\ &X = A_2 \sin(\gamma_2 (w_2 - x)) \quad , \quad w_1 < x \le w_2 \end{aligned} \tag{A-7}$$

in which

$$\gamma_1^2 = \tfrac{\lambda}{D_1} - \alpha_1^2 \quad , \quad \gamma_2^2 = \tfrac{\lambda}{D_2} - \alpha_2^2 \tag{A-8}$$

The above form of X automatically satisfies b.c.'s (A-2) and (A-3). Then to satisfy boundary conditions (A-5) and (A-4), we require,

$$N_1 A_1 \sin(\gamma_1 w_1) = N_2 A_2 \sin(\gamma_2 (w_2 - w_1)) \tag{A-9}$$

and

$$D_1 A_1 \gamma_1 \cos(\gamma_1 w_1) = -D_2 A_2 \gamma_2 \cos(\gamma_2 (w_2 - w_1)) \tag{A-10}$$

writing these two equations in matrix form,

$$\begin{bmatrix} D_1 \gamma_1 \cos(\gamma_1 w_1) & D_2 \gamma_2 \cos(\gamma_2 (w_2 - w_1)) \\ -N_1 \sin(\gamma_1 w_1) & N_2 \sin(\gamma_2 (w_2 - w_1)) \end{bmatrix} \begin{bmatrix} A_1 \\ A_2 \end{bmatrix} = \begin{bmatrix} 0 \\ 0 \end{bmatrix} \tag{A-11}$$

To obtain non-trivial solutions we require,

$$\begin{aligned} |M| \quad = \quad & D_1 \gamma_1 N_2 \cos(\gamma_1 w_1) \sin(\gamma_2 (w_2 - w_1)) + \\ & D_2 \gamma_2 N_1 \sin(\gamma_1 w_1) \cos(\gamma_2 (w_2 - w_1)) = 0 \end{aligned} \tag{A-12}$$

However we also know, from (A-8) that

$$\gamma_2^2 = \frac{D_1}{D_2}(\gamma_1^2 + \alpha_1^2) - \alpha_2^2 \tag{A-13}$$

Substituting (A-13) into (A-12) yields the transcendental equation from which the eigenvalues may be found. If we label the solutions $\gamma_{1,n}$, $n = 1, 2, 3..$, then the eigenvalues are given by

$$\lambda_n = D_1(\gamma_{1,n}^2 + \alpha_1^2) \quad , \quad n = 1, 2, 3.. \tag{A-14}$$

Associated with each eigenvalue, we may select the corresponding eigenvector, using (A-9), as:

$$\begin{bmatrix} A_1 \\ A_2 \end{bmatrix} = \begin{bmatrix} N_2 \sin(\gamma_2 (w_2 - w_1)) \\ N_1 \sin(\gamma_1 w_1) \end{bmatrix} \tag{A-15}$$

giving us the eigenfunctions

$$X_n(x) \quad = \quad \begin{cases} N_2 \sin(\gamma_{2,n}(w_2 - w_1)) \sin(\gamma_{1,n} x) \quad , \quad 0 \le x \le w_1 \\ N_1 \sin(\gamma_{1,n} w_1) \sin(\gamma_{2,n}(w_2 - x)) \quad , \quad w_1 < x \le w_2 \end{cases} \quad , \quad n = 1, 2, 3, .. \tag{A-16}$$

The remaining interval, $\frac{1}{\tau_1} < \lambda \leq \frac{1}{\tau_2}$ (we assume $\frac{1}{\tau_2} > \frac{1}{\tau_1}$, because that is the case for a typical device), over which it is possible to find eigenvalues is the one in which one set of roots are real, but the other set are complex. Writing the general solution as,

$$\begin{aligned} X &= A_1 \sin(\gamma_1 x) \quad , \quad 0 \leq x \leq w_1 \\ X &= A_2 \sinh(\gamma_2 (w_2 - x)) \quad , \quad w_1 < x \leq w_2 \end{aligned} \tag{A-17}$$

in which

$$\gamma_1^2 = \frac{\lambda}{D_1} - \alpha_1^2 \quad , \quad \gamma_2^2 = \alpha_2^2 - \frac{\lambda}{D_2} \tag{A-18}$$

and proceeding as in the previous case, we find that the equation

$$\begin{aligned} |M| \quad = \quad & D_1 \gamma_1 N_2 \cos(\gamma_1 w_1) \sinh(\gamma_2 (w_2 - w_1)) + \\ & D_2 \gamma_2 N_1 \sin(\gamma_1 w_1) \cosh(\gamma_2 (w_2 - w_1)) = 0 \end{aligned} \tag{A-19}$$

determines whether or not any eigenvalues exist. We may derive a simple condition on the parameters, which enables us to exclude eigenvalues for $\frac{1}{\tau_1} < \lambda \leq \frac{1}{\tau_2}$. In particular, by virtue of the fact that $|M| > 0$ whenever $0 < \gamma_1 w_1 < \frac{\pi}{2}$, we may conclude no eigenvalues exist if $\frac{D_1 \pi^2}{4 w_1^2} + \frac{1}{\tau_1} > \frac{1}{\tau_2}$. By way of an example, for the parameter set given in Table 2 in Section 3.1 there are no non-trivial solutions. However, if we lower the lifetime in the n^+ region to $\tau_2 = 2.0 \times 10^{-9}$ s, then the length of this interval is greatly increased, allowing the trigonometric functions in (A-19) to fluctuate over a longer period. For this reduced lifetime, we do find one eigenvalue, $\lambda = 3.08 \times 10^8$, and, consequently, one eigenfunction of the form (A-17). For other parameter sets it is also possible for there to be more than one eigenvalue, but only a finite number: missing such eigenvalues will lead to an incomplete set of eigenfunctions and produce erroneous results. Dealing with these additional eigenfunction(s) does not present any major problems. However, to simplify the following formulas we shall assume that the only eigenfunctions correspond to the case when $\lambda > \max\{\frac{1}{\tau_1}, \frac{1}{\tau_2}\}$.

The solution functions are orthogonal with respect to the weighted inner product

$$\langle f \cdot g \rangle = \int_0^{w_1} f g dx + \frac{N_2}{N_1} \int_{w_1}^{w_2} f g dx \tag{A-20}$$

while the norm squared is given by,

$$\begin{aligned} \langle X_n(x) \cdot X_n(x) \rangle \quad = \quad & [N_2 \sin(\gamma_{2,n}(w_2 - w_1))]^2 \int_0^{w_1} \sin^2(\gamma_{1,n} x) dx + \\ & \tfrac{N_2}{N_1} [N_1 \sin(\gamma_{1,n} w_1)]^2 \int_{w_1}^{w_2} \sin^2(\gamma_{2,n}(w_2 - x)) dx \end{aligned}$$

Noting that the norm squared is not a function of x,

$$\begin{aligned} \|X_n\|^2 \quad = \quad & N_2^2 \sin^2(\gamma_{2,n}(w_2 - w_1)) \left[\tfrac{w_1}{2} - \tfrac{\sin(2\gamma_{1,n} w_1)}{4\gamma_{1,n}} \right] + \\ & \tfrac{N_2}{N_1} N_1^2 \sin^2(\gamma_{1,n} w_1) \left[\tfrac{w_2 - w_1}{2} - \tfrac{\sin(2\gamma_{2,n}(w_2 - w_1))}{4\gamma_{2,n}} \right] \end{aligned} \tag{A-21}$$

To solve the transient BVP we define the finite Fourier transform pair via

$$\bar{u}_n(t) = \langle u(x,t) \cdot X_n(x) \rangle = \int_0^{w_1} u(x,t) X_n(x) dx + \frac{N_2}{N_1} \int_{w_1}^{w_2} u(x,t) X_n(x) dx \tag{A-22}$$

with inversion formula

$$u(x,t) = \sum_{n=1}^{\infty} \frac{\bar{u}_n(t) X_n(x)}{\|X_n\|^2} \tag{A-23}$$

Applying this transform to our BVP, yields the ODE,

$$\frac{d}{dt}\bar{u}_n(t) = -\lambda_n \bar{u}_n(t) + w_n g(t) \qquad , \qquad n = 1,2,3... \tag{A-24}$$

with initial condition $\bar{u}_n(0) = 0$, and in which

$$\begin{aligned} w_n = \langle 1 \cdot X_n(x) \rangle &= \int_0^{w_1} X_n(x) dx + \tfrac{N_2}{N_1} \int_{w_1}^{w_2} X_n(x) dx \\ &= N_2 \Big[\sin(\gamma_{2,n}(w_2 - w_1)) \tfrac{1-\cos(\gamma_{1,n} w_1)}{\gamma_{1,n}} \\ &\quad + \sin(\gamma_{1,n} w_1) \tfrac{1-\cos(\gamma_{2,n}(w_2 - w_1))}{\gamma_{2,n}} \Big] \end{aligned} \tag{A-25}$$

The solution of the relevant initial value problem is given by

$$\bar{u}_n(t) = w_n \int_0^t g(v) e^{-\lambda_n (t-v)} dv \tag{A-26}$$

Substituting equation (A-26) into equation (A-23) we obtain our general solution, representing the excess carrier density within the undepleted nn^+ region of the device.

$$u(x,t) = \sum_{n=1}^{\infty} w_n \int_0^t g(v) e^{-\lambda_n (t-v)} dv \frac{X_n(x)}{\|X_n\|^2} \tag{A-27}$$

The associated photocurrent is given by

$$\begin{aligned} J_{pp}(t) &= qD_1 \left. \tfrac{\partial u}{\partial x} \right|_{x=0} \\ &= qD_1 \sum_{n=1}^{\infty} w_n \int_0^t g(v) e^{-\lambda_n (t-v)} dv \tfrac{X_n'(0)}{\|X_n\|^2} \end{aligned} \tag{A-28}$$

For the case where $g(t) = g$ (a constant) equation (A-27) reduces to

$$u(x,t) = g \sum_{n=1}^{\infty} w_n \frac{1 - e^{-\lambda_n t}}{\lambda_n} \frac{X_n(x)}{\|X_n\|^2} \tag{A-29}$$

Observe

$$u(x,t) = g\sum_{n=1}^{\infty}\frac{w_n}{\lambda_n}\frac{X_n(x)}{\|X_n\|^2} - g\sum_{n=1}^{\infty}w_n\frac{e^{-\lambda_n t}}{\lambda_n}\frac{X_n(x)}{\|X_n\|^2} \tag{A-30}$$

from which it can be readily seen, that

$$u(x,\infty) = g\sum_{n=1}^{\infty}\frac{w_n}{\lambda_n}\frac{X_n(x)}{\|X_n\|^2} \tag{A-31}$$

and so we may replace $u(x,\infty) = U(x)$ (say) with the formula obtained from substituting (18) and (19) into (14) : the steady-state solution, giving us

$$u(x,t) = U(x) - g\sum_{n=1}^{\infty}w_n\frac{e^{-\lambda_n t}}{\lambda_n}\frac{X_n(x)}{\|X_n\|^2} \tag{A-32}$$

The associated photocurrent is given by

$$J_{pp}(t) \quad = \quad qD_1\alpha_1\left[A + g\tau_1 - g\frac{N_2}{\alpha_1}\sum_{n=1}^{\infty}w_n\frac{e^{-\lambda_n t}}{\lambda_n}\frac{\sin(\gamma_{2,n}(w_2-w_1))\gamma_{1,n}}{\|X_n\|^2}\right] \tag{A-33}$$

For the case where the carrier generation rate is a step function,

$$g(t) = \begin{cases} g \quad , \quad 0 \le t \le t' \\ \\ 0 \quad , \quad t' < t < \infty \end{cases} \tag{A-34}$$

equation (A-27) reduces to

$$u(x,t) = \begin{cases} U(x) - g\sum_{n=1}^{\infty}w_n\frac{e^{-\lambda_n t}}{\lambda_n}\frac{X_n(x)}{\|X_n\|^2} \quad , \quad 0 \le t \le t' \\ \\ g\sum_{n=1}^{\infty}w_n\frac{e^{-\lambda_n(t-t')}-e^{-\lambda_n t}}{\lambda_n}\frac{X_n(x)}{\|X_n\|^2} \quad , \quad t' < t < \infty \end{cases} \tag{A-35}$$

and the associated photocurrent is given by

$$J_{pp}(t) = \begin{cases} qD_1\alpha_1\left[A + g\tau_1 - g\frac{N_2}{\alpha_1}\sum_{n=1}^{\infty}w_n\frac{e^{-\lambda_n t}\sin(\gamma_{2,n}(w_2-w_1))\gamma_{1,n}}{\lambda_n\|X_n\|^2}\right], \quad 0 \le t \le t' \\ \\ qD_1N_2g\sum_{n=1}^{\infty}w_n\frac{e^{-\lambda_n(t-t')}-e^{-\lambda_n t}}{\lambda_n}\frac{\sin(\gamma_{2,n}(w_2-w_1))\gamma_{1,n}}{\|X_n\|^2}, \qquad t' < t < \infty \end{cases} \tag{A-36}$$

We note that if there are any eigenvalues for the case when $\frac{1}{\tau_1} < \lambda \le \frac{1}{\tau_2}$, then the corresponding eigenfunctions are (still) orthogonal to each other and the ones above w.r.t. to the same weighted inner product (A-20), however, the formulas for $\|X_n\|^2$ and w_n would have to be modified.

B Limiting Behavior of Photocurrent Solutions

There are two limiting cases that serve as a check for the analytic photocurrent solution. Our steady-state photocurrent should approach the exact steady-state solution given in [3] as $w_2 \to \infty$. As a second check of our photocurrent solution, we observe that as the parameters in the substrate, $x \in [w_1, w_2]$, approach those of the lower-doped region ($x \in [0, w_1]$), we expect our solutions to approach that for a homogeneous region as published in [16]. In particular, the steady-state solution for a constant pulse should approach the solution of [4].

B.1 Comparison with the Long, Florian, and Casey [3] Steady-State Solution

If we look at the case when $w_2 \to \infty$

$$A_\infty = \lim_{w_2 \to \infty} g \frac{N_2 \frac{S_2(w_1)}{S_2(w_1)} \left[D_2 \tau_2 G_2'(w_1) - D_1 \tau_1 G_1'(w_1)\right] - D_2 \frac{S_2'(w_1)}{S_2(w_1)} \left[N_2 \tau_2 G_2(w_1) - N_1 \tau_1 G_1(w_1)\right]}{D_1 N_2 S_1'(w_1) - N_1 D_2 S_1(w_1) \frac{S_2'(w_1)}{S_2(w_1)}} \tag{B-1}$$

then using the results

$$\lim_{w_2 \to \infty} \frac{S_2'(w_1)}{S_2(w_1)} = -\alpha_2 \quad , \quad \lim_{w_2 \to \infty} G_2'(w_1) = 0 \quad , \quad \lim_{w_2 \to \infty} G_2(w_1) = 1 \tag{B-2}$$

it follows that

$$A_\infty = g \frac{N_2 \left[-D_1 \tau_1 G_1'(w_1)\right] + D_2 \alpha_2 \left[N_2 \tau_2 - N_1 \tau_1 G_1(w_1)\right]}{D_1 N_2 S_1'(w_1) + \alpha_2 N_1 D_2 S_1(w_1)} \tag{B-3}$$

so

$$A_\infty = g \frac{-D_1 \tau_1 G_1'(w_1) + D_2 \alpha_2 \tau_2 - D_2 \alpha_2 \frac{N_1}{N_2} \tau_1 G_1(w_1)}{D_1 \alpha_1 \cosh(\alpha_1 w_1) + \alpha_2 \frac{N_1}{N_2} D_2 \sinh(\alpha_1 w_1)} \tag{B-4}$$

hence

$$A_\infty = g \frac{D_2 \alpha_2 \left[\frac{N_1}{N_2} \tau_1 \left[e^{-\alpha_1 w_1} - 1\right] + \tau_2\right] - D_1 \tau_1 \alpha_1 e^{-\alpha_1 w_1}}{D_1 \alpha_1 \cosh(\alpha_1 w_1) + \alpha_2 \frac{N_1}{N_2} D_2 \sinh(\alpha_1 w_1)} \tag{B-5}$$

This is equation (12) in [3]. As discussed previously, the transient solution in [3] is solved assuming that there is no current from the n^+ doped to the n region. Since our transient solution did not need to make this assumption, we have not attempted to compare to this solution in the limit.

B.2 Comparison with the Stuetzer [4] Steady-State Solution

In this section we assume the parameters in the substrate, $x \in [w_1, w_2]$ approach those of the epitaxial region ($x \in [0, w_1]$). In this case, the steady-state photocurrent solution to a constant pulse, $g(t) = g, t \geq 0$, should approach that of [4]. We show this to be case by computing the limit of the minority carrier photocurrent density at both the n contact ($x = 0$) and the n^+ contact ($x = w_2$). At the n contact, from equation (14), and using the notation $lim_{n^+ \to n}$ to mean $lim_{(n^+ \text{ doping}) \to (n \text{ doping})}$, $lim_{D_2 \to D_1}$, and $lim_{\tau_2 \to \tau_1}$, simultaneously,

$$
\begin{aligned}
lim_{n+\to n} J_{pp+}(\infty) &= qD_1\alpha_1\left[lim_{n+\to n}A + g\tau_1\right] \\
&= qgL_p\left[\frac{-\sinh(\alpha_1(w_2-w_1))\left(e^{-\alpha_1(w_2-w_1)}+e^{-\alpha_1 w_1}\right)}{\sinh(\alpha_1 w_2)}\right. \\
&\quad \left. + \frac{\cosh(\alpha_1(w_2-w_1))\left(e^{-\alpha_1 w_1}-e^{-\alpha_1(w_2-w_1)}\right)}{\sinh(\alpha_1 w_2)} + 1\right] \\
&= qgL_p\left[\frac{1}{\sinh(\alpha_1 w_2)}\left(-1+e^{-\alpha_1 w_2}\right)+1\right] \\
&= qgL_p\left[\coth(\alpha_1 w_2) - \frac{1}{\sinh(\alpha_1 w_2)}\right]
\end{aligned}
$$

where we also use equation (18) and where $L_p = \sqrt{D_1\tau_1}$ is the diffusion length. At the $n+$ contact, beginning with equation (14), and using the same limit notation, we are again led to the same equations as above. These equations both agree with the Stuetzer solution, equation (21) of [16], when the ohmic field is assumed zero. This analysis serves as a mathematical validation for both constants A and B. The TCAD results of section 3.1 serve as a further validation.

C Evaluation of the Excess Carrier and Photocurrent Densities for a General Piecewise Linear $g(t)$

Suppose that the generation function $g(t)$ is given by a discrete data set: $(t_i, g(t_i) = g_i)$, $i = 0, 1, 2, 3, \ldots$ in which $t_{i+1} - t_i$ is *small,* (for all i). Then we can represent our data set with the piecewise linear function

$$g(t) = \begin{cases} g_0 + m_0(t - t_0) & , \quad 0 \le t \le t_1 \\ g_1 + m_1(t - t_1) & , \quad t_1 < t \le t_2 \\ & \vdots \\ g_{j-1} + m_{j-1}(t - t_{j-1}) & , \quad t_{j-1} < t \le t_j \end{cases}$$

in which $m_{j-1} = \frac{g_j - g_{j-1}}{t_j - t_{j-1}}$

Labelling the integral in equation (21) as $I_n(t)$, it follows that at the end of the first time interval: $0 = t_0 \le t \le t_1$.

$$\begin{aligned} I_n(t_1) = \int_0^{t_1} g(v) e^{-\lambda_n (t_1 - v)} dv &= \int_0^{t_1} \left[g_0 + m_0(v - t_0) \right] e^{-\lambda_n (t_1 - v)} dv \\ &= \frac{g_0 + m_0(t_1 - t_0)}{\lambda_n} - \frac{m_0}{\lambda_n^2} \\ &\quad - g_0 \frac{e^{-\lambda_n (t_1 - t_0)}}{\lambda_n} + m_0 \frac{e^{-\lambda_n (t_1 - t_0)}}{\lambda_n^2} \end{aligned} \tag{C-1}$$

Similarly

$$\begin{aligned} I_n(t_2) = \int_0^{t_2} g(v) e^{-\lambda_n (t_2 - v)} dv &= e^{-\lambda_n (t_2 - t_1)} I_n(t_1) \\ &\quad + \frac{g_1 + m_1(t_2 - t_1)}{\lambda_n} - \frac{m_1}{\lambda_n^2} \\ &\quad - g_1 \frac{e^{-\lambda_n (t_2 - t_1)}}{\lambda_n} + m_1 \frac{e^{-\lambda_n (t_2 - t_1)}}{\lambda_n^2} \end{aligned} \tag{C-2}$$

And, continuing:

$$\begin{aligned} I_n(t_j) &= e^{-\lambda_n (t_j - t_{j-1})} I_n(t_{j-1}) \\ &\quad + \frac{g_{j-1} + m_{j-1}(t_j - t_{j-1})}{\lambda_n} - \frac{m_{j-1}}{\lambda_n^2} \\ &\quad - g_{j-1} \frac{e^{-\lambda_n (t_j - t_{j-1})}}{\lambda_n} + m_{j-1} \frac{e^{-\lambda_n (t_j - t_{j-1})}}{\lambda_n^2} \end{aligned} \tag{C-3}$$

Therefore

$$u(x, t_j) = \sum_{n=1}^{\infty} w_n I_n(t_j) \frac{X_n(x)}{\|X_n\|^2} \tag{C-4}$$

and the associated photocurrent is given by:

$$\begin{aligned} J_{pp}(t_j) &= qD_1 \left.\frac{\partial u}{\partial x}\right|_{x=0} \\ &= qD_1 \sum_{n=1}^{\infty} w_n I_n(t_j) \frac{X_n'(0)}{\|X_n\|^2} \end{aligned} \tag{C-5}$$

hence

$$\begin{aligned} J_{pp}(t_j) &= qD_1 \sum_{n=1}^{\infty} w_n \frac{g_{j-1}+m_{j-1}(t_j-t_{j-1})}{\lambda_n} \frac{X_n'(0)}{\|X_n\|^2} \\ &\quad +qD_1 \sum_{n=1}^{\infty} w_n \left[e^{-\lambda_n(t_j-t_{j-1})} I_n(t_{j-1}) - \frac{m_{j-1}}{\lambda_n^2} \right] \frac{X_n'(0)}{\|X_n\|^2} \\ &\quad -qD_1 \sum_{n=1}^{\infty} w_n \left[g_{j-1} \frac{e^{-\lambda_n(t_j-t_{j-1})}}{\lambda_n} - m_{j-1} \frac{e^{-\lambda_n(t_j-t_{j-1})}}{\lambda_n^2} \right] \frac{X_n'(0)}{\|X_n\|^2} \end{aligned} \tag{C-6}$$

However, we also know that

$$\sum_{n=1}^{\infty} \frac{w_n}{\lambda_n} \frac{X_n'(0)}{\|X_n\|^2} = \left[\frac{A}{g} + \tau_1 \right] \alpha_1$$

with the definitions of A and α_1 given in Section 2.1.

Therefore, we may replace the slowest converging sum with the above to obtain,

$$\begin{aligned} J_{pp}(t_j) &= qD_1 \left[g_{j-1} + m_{j-1}(t_j - t_{j-1}) \right] \left[\frac{A}{g} + \tau_1 \right] \alpha_1 \\ &\quad +qD_1 \sum_{n=1}^{\infty} w_n \left[e^{-\lambda_n(t_j-t_{j-1})} I_n(t_{j-1}) - \frac{m_{j-1}}{\lambda_n^2} \right] \frac{X_n'(0)}{\|X_n\|^2} \\ &\quad -qD_1 \sum_{n=1}^{\infty} w_n \left[g_{j-1} \frac{e^{-\lambda_n(t_j-t_{j-1})}}{\lambda_n} - m_{j-1} \frac{e^{-\lambda_n(t_j-t_{j-1})}}{\lambda_n^2} \right] \frac{X_n'(0)}{\|X_n\|^2} \end{aligned} \tag{C-7}$$

DISTRIBUTION:

1 Bert Kerr
Mathematics Department
New Mexico Institute of Mining and Technology
801 Leroy Place
Socorro, NM 87801

1 Carl Axness (retired)
c/ Trafalgar 70, bajo
03004 Alicante
Spain

1 Nick Hitchon
Electrical and Computer Engineering
University of Wisconsin
1415 Engineering Drive
Madison, WI 53706

1 Al Lehnen
Mathematics Department
Madison Area Technical College
3550 Anderson Street
Madison, WI 53704

1 Lloyd Massengill
Vanderbilt University
VU Station B 351683
Nashville, TN 37235-1683

1 James Petrosky
The Air Force Institute of Technology
Department of Engineering Physics
2950 Hobson Way
WPAFB OH, 45433

1 Jaijeet Roychowdhury
Electrical Engineering and Computer Sciences Department
545E Cory Hall
University of California-Berkeley
Berkeley, CA 94720

1	MS 0110	Mark Hedemann, 01230
1	MS 0348	John Dye, 05351
1	MS 0352	Charles Hembree, 01344
1	MS 0386	Joseph Castro, 01445
1	MS 0405	Ben Long, 00432
1	MS 0405	Glenn Rice, 00432
1	MS 0457	Robert Paulsen, 02211

1 MS 0525 Steven Wix, 01734
1 MS 0525 Teresa Gutierrez, 01734
1 MS 0529 Steven Dunlap, 05335
1 MS 0828 Vicente Romero, 01544
1 MS 0829 Brian Rutherford, 00431
1 MS 1056 Edward Bielejec, 01111
1 MS 1056 Gyorgy Vizkelethy, 01111
1 MS 1056 William Wampler, 01111
1 MS 1071 David Sandison, 01740
1 MS 1072 Jeffrey Black, 01752
1 MS 1072 Nathan Nowlin, 01754
1 MS 1083 Paul Dodd, 01752
1 MS 1085 Charles Sullivan, 01742
1 MS 1085 Albert G. Baca, 01742
1 MS 1138 Biliana Paskaleva, 06923
1 MS 1146 Donald King, 01384
1 MS 1146 Patrick Griffin, 02200
1 MS 1159 James Bryson, 01344
1 MS 1159 Kyle Mcdonald, 01344
1 MS 1159 Victor Harper-Slaboszewicz, 01344
1 MS 1167 Michael McLain, 01343
1 MS 1179 Grant Heffelfinger, 01340
1 MS 1179 Harold Hjalmarson, 01341
1 MS 1179 Leonard Lorence, 01341
1 MS 1318 Bruce Hendrickson, 01440
1 MS 1318 Robert Hoekstra, 01426
1 MS 1318 Russell Hooper, 01445
1 MS 1318 Timothy Trucano, 01441
1 MS 1322 Gary Hennigan, 01425
1 MS 1322 John Aidun, 01425
1 MS 1322 Ting Mei, 01445
1 MS 1323 Eric Keiter, 01445
1 MS 1323 Eric Rankin, 01445
1 MS 1323 Heidi Thornquist, 01445
5 MS 1323 Jason Verley, 01445
1 MS 1323 Richard Schiek, 01445
1 MS 1323 Scott Hutchinson, 01445
1 MS 1323 Thomas Russo, 01445
1 MS 1415 Robert Fleming, 01123
1 MS 1427 Charles Barbour, 01100
1 MS 9007 Cheryl Lam, 08225

1	MS 9007	Dean Clark, 08225
1	MS 9154	Brian E. Owens, 08244
1	MS 9154	William Ballard, 08200
1	MS 9159	Genetha Gray, 08954
1	MS 0899	RIM-Reports Management, 09532 (electronic copy)

Sandia National Laboratories